Earth and Planetary Science Letters
March 2018, Volume 486 Pages 155-165
http://dx.doi.org/10.1016/j.epsl.2018.01.011
http://archimer.ifremer.fr/doc/00425/53625/
© 2018 Elsevier B.V. All rights reserved.

Achimer
http://archimer.ifremer.fr

Tsunamigenic earthquake simulations using experimentally derived friction laws

Murphy Shane [1, 2, *], Di Toro G. [3, 4], Romano F. [1], Scala A [1], Lorito S. [1], Spagnuolo E. [1], Aretusini S. [3], Festa G. [5], Piatanesi A. [1], Nielsen S. [6]

[1] Istituto Nazionale di Geofisica e Vulcanologia, Rome, Italy
[2] Ifremer, Plouzané, France
[3] University of Manchester, Manchester, United Kingdom
[4] Università degli Studi di Padova, Padua, Italy
[5] Università di Napoli Federico II, Naples, Italy
[6] Durham University, Durham, United Kingdom

* Corresponding author : Shane Murphy, email address : shane.murphy@ifremer.fr

Abstract :

Seismological, tsunami and geodetic observations have shown that subduction zones are complex systems where the properties of earthquake rupture vary with depth as a result of different pre-stress and frictional conditions. A wealth of earthquakes of different sizes and different source features (e.g. rupture duration) can be generated in subduction zones, including tsunami earthquakes, some of which can produce extreme tsunamigenic events. Here, we offer a geological perspective principally accounting for depth-dependent frictional conditions, while adopting a simplified distribution of on-fault tectonic pre-stress.

We combine a lithology-controlled, depth-dependent experimental friction law with 2D elastodynamic rupture simulations for a Tohoku-like subduction zone cross-section. Subduction zone fault rocks are dominantly incohesive and clay-rich near the surface, transitioning to cohesive and more crystalline at depth. By randomly shifting along fault dip the location of the high shear stress regions (“asperities”), moderate to great thrust earthquakes and tsunami earthquakes are produced that are quite consistent with seismological, geodetic, and tsunami observations. As an effect of depth-dependent friction in our model, slip is confined to the high stress asperity at depth; near the surface rupture is impeded by the rock-clay transition constraining slip to the clay-rich layer. However, when the high stress asperity is located in the clay-to-crystalline rock transition, great thrust earthquakes can be generated similar to the Mw 9 Tohoku (2011) earthquake.

Please note that this is an author-produced PDF of an article accepted for publication following peer review. The definitive publisher-authenticated version is available on the publisher Web site.

Highlights

► 2D dynamic rupture simulation of earthquakes on the Tohoku fault. ► Model contains laboratory derived seismic friction laws and subduction geology. ► Different earthquake types have different depth domains similar to observations. ► Megathrust events occur when asperity is located in the clay-to-rock transition.

Keywords : subduction zone, megathrust, dynamic rupture, rock physics experiments, tsunami earthquake

Please note that this is an author-produced PDF of an article accepted for publication following peer review. The definitive publisher-authenticated version is available on the publisher Web site.

1. Introduction

Seismological, geodetic, and tsunami observations have shown that subduction zones are complex systems where the properties of earthquake rupture vary with depth (Lay et al., 2012). For example, earthquake duration normalized for event size has been observed to decrease with depth; this recurrent feature has been attributed to depth varying shear modulus and / or stress drop for individual earthquakes (Bilek and Lay, 1999; Bilek et al., 2016; Geist and Bilek, 2001). Depth variation in subduction ruptures is, for example, evident when comparing the different historical earthquakes that occurred off the Pacific coast of Tohoku region in Japan (Fig. 1). A number of major (M_w 7-7.9) thrust earthquakes mostly slipped within a depth range of 10 – 40 km. These events involved individual patches of concentrated slip implying

50 the breaking of at least one prominent, high stress asperity (Shao et al., 2011;
51 Yamanaka and Kikuchi, 2004). Conversely, the 1896 Meiji event (M 8.2 – 8.4), likely
52 involved slip primarily at the base of the shallow accretionary wedge or beneath it.
53 This earthquake produced a disproportionately large tsunami relative to its moment
54 magnitude, possibly making it a potential 'tsunami earthquake' (Kanamori, 1972).
55 The great M_w 9.0 2011 Tohoku earthquake nucleated at ~20 – 25 km depth, and
56 produced slip at traditionally expected depths while also realising a substantial
57 amount of slip all the way to the trench (i.e., at less than 10 km depth) (Chu et al.,
58 2011; Ide et al., 2011; Romano et al., 2014).

59 Numerical models of the dynamic rupture process have successfully described
60 either individual types of earthquakes, for example the Tohoku event (Kozdon and
61 Dunham, 2013; Noda and Lapusta, 2013), or both thrust and tsunami earthquakes in
62 the same model (Mitsui and Yagi, 2013). Numerical models coupled with the rate-
63 and-state friction law have been used to reproduce full seismic cycles for subduction
64 environments. However, this comes at the expense of either failing to account for
65 geometry / free surface effects and inhomogeneity in the material surrounding the
66 fault (Cubas et al., 2015; Noda and Lapusta, 2013), or by simplifying wave
67 propagation to static stress changes on the fault plane (Shibazaki et al., 2011). Fully
68 dynamic simulations including a free surface and variable geometry have tended to
69 focus on specific rupture features of the Tohoku earthquake such as the slip in the
70 trench or long period guided wave propagation in the ocean (Hirono et al., 2016;
71 Huang et al., 2013; Kozdon and Dunham, 2014). Depth dependent changes in
72 frictional parameters have been tested using rate-and-state models for the 2011
73 Tohoku (Kozdon and Dunham, 2013). However, to our knowledge, no numerical
74 model has been able to reproduce a range of different observed earthquakes types

(e.g. Fig. 1) while at the same time accounting for the fault geometry and complex structure as proposed here.

The focus of this study is to provide a simple yet geologically consistent model that reconciles the different observed earthquake types with fault properties from independent theoretical and laboratory studies. We focus our investigation on the aspect of rupture dynamics due to depth-dependent frictional conditions focusing on a specific time window of the seismic cycle including the sub-seismic frictional properties of the fault materials (Den Hartog et al., 2012). Hence, the friction law parameters were chosen based on available geological and geophysical constraints. On the other hand, investigating inter-seismic and nucleation processes is beyond the scope of this study. As a consequence, the set up for the numerical model was simplified, particularly as far as the initial stress distribution is concerned. While the initial stress is heterogeneous, being the derivative of a composite slip model (Murphy et al., 2016), it is highly localized. Moreover, since a 2D model is used, we do not address the influence of lateral variations on rupture features.

2. Numerical Model

We modelled the earthquake rupture dynamics (Festa and Vilotte, 2006) on a 2D cross-section through a Tohoku-like fault (Figs. 2a-d). Dynamic rupture is simulated using a 2D non-smooth spectral element method (Festa and Vilotte, 2005). The curved fault geometry is based on Slab 1.0 (Hayes et al., 2012) which has been slightly modified so that the subduction interface extends to the surface. The media is heterogeneous with the layers and their elastic properties (described in Fig. 2 and Table S1 in *Supplementary Material*) based on a seismic survey in the zone of the 2011 Tohoku earthquake (Miura et al., 2005).

100

101 ***2.1 Laboratory derived thermal weakening friction law***

102 A thermal slip weakening empirical friction law was used in all simulations
103 which is particularly suitable for representing dynamic weakening observed in a
104 regime of slip velocities that rapidly accelerate to seismic slip rates. There are a
105 number of other empirical friction laws (e.g., linear slip weakening (Ida, 1972); rate-
106 and-state (Dieterich, 1979; Ruina, 1983)). We have chosen the thermal weakening
107 friction law as it is based on rock physics experiments performed at slip-rates
108 expected during large earthquakes using materials typical in subduction zones.

109 This law is based on laboratory observations of the evolution of friction with
110 slip in a rotary shear machine where cohesive (serpentinites, peridotites, gabbros,
111 basalts, marbles, granitoids, sandstones, etc.) and non-cohesive (clay-rich gouges,
112 serpentinite gouges, basalt gouges, etc.) rocks were tested over a quite large range of
113 slip rates (0.1 to 6.5 m/s), accelerations (0.5 to 65 m/s^2), normal stresses (5 to 95
114 MPa), ambient conditions (room humidity to fluid saturated) and displacements (0.3
115 to 50 m) expected during moderate to large earthquakes (Di Toro et al., 2011). A
116 common feature from this extensive set of experiments is that the evolution of friction
117 with slip can be described by an exponential decay to a first order approximation.
118 This dependency is defined as:

119

$$\mu\,(\delta) = \mu_d + (\mu_s - \mu_d)e^{\frac{-\delta}{d_{th}}} \qquad \text{(Eq. 1)}$$

120

121 where μ_s and μ_d are the static and dynamic friction coefficients, respectively, and
122 depend on material type. The co-seismic slip is δ and d_{th} the thermal weakening
123 distance. For a suite of experiments performed at a variety of slip rates and normal
124 stresses, d_{th} was shown to have an inverse relationship with the normal stress σ_n:

$$d_{th} = \alpha \, \|\sigma_n\|^{-\beta} \qquad \text{(Eq. 2)}$$

with α ranging between 3 - 78 depending on material type (Di Toro et al., 2011) and β = 1 (Nielsen et al., 2010). This friction law produces a similar exponential evolution of fault strength with slip to that observed by Hirono et al. (2016) whose numerically modelled thermal pressurization on the Japan Trench using expected permeability and porosity for the region.

2.2 Variation in fault material

Depth dependent frictional parameters were chosen based on expected dominant rock types in mega-thrust environments (Hacker et al., 2003a; 2003b; Kimura et al., 2012; Meneghini et al., 2010). Initially unconsolidated and, in the case of Tohoku, clay-rich sediments (Chester et al., 2013), undergo compaction, dehydration, diagenesis and metamorphism into crystalline rocks (phyllites, schists, calc-schists, marbles, quartzites, etc.) due to increasing pressure and temperature during burial (Hacker et al., 2003b; 2003a; Hyndman et al., 1997; Ikari et al., 2007; Kimura et al., 2012). Consequently, high velocity experiments on peridotite (Del Gaudio et al., 2009) were taken as a proxy for mantle rock (i.e., μ_s = 0.7, μ_d = 0.25, α = 78), however gabbro, basalts and serpentinite have similar frictional properties when sheared under seismic deformation conditions (Niemeijer et al., 2011; Proctor et al., 2014; Violay et al., 2014). For clay-like material the static and dynamic coefficients of friction were set to 0.25 and 0.1 respectively based on experiments performed under room humidity conditions and in the presence of liquid water

150 (Remitti et al., 2015; Sawai et al., 2014; Ujiie et al., 2013). Experimental studies from
151 literature were used to determine the α value used for the clay-like material in the
152 numerical model (see Fig 3 and Table S3 in Supplementary Material). Most of the
153 latter experiments were performed at room humidity on a variety of different clay
154 minerals and under increasing normal stresses. Ideally, data from experiments on
155 unconsolidated wet clay materials would be used. However, experiments at high
156 normal stress (> 20 MPa) are very challenging on these materials and not enough data
157 exist to calculate the variation of d_{th} with normal stress. Setting $\beta = 1$ based on
158 theoretical findings (Nielsen et al., 2010), $\alpha = 3.712$ provided the best fit for
159 equation 2 to the experimental data (see Fig. 3) with a R-square of 0.735 and a 95%
160 confidence bounds of 3.32 to 4.11. Below 40 km d_{th} was artificially increased to 20 m
161 in order to act as a numerical barrier to rupture at the bottom of the fault. This depth
162 was chosen as it corresponds to the depth at which co-seismic slip in the 2011 M_w 9.0
163 Tohoku earthquake rapidly decreased and the largest post-seismic slip occurred
164 (Ozawa et al., 2011). This is also the estimated depth where creep begins (Freed,
165 2005).

166 Using an effective basal friction of 0.03, thermal modelling of the Tohoku
167 fault (Kimura et al., 2012) places the 50°C isotherm at 10 km depth and 150°C
168 isotherm at a depth of 20 km. Guided by these findings, we defined the frictional
169 parameters above 2 km as clay-like, with a linear transition to rock-like frictional
170 parameters in the 12-20 km depth range. This interval accounts for peak dehydration
171 due to opal to quartz and smectite to illite conversion rates estimated to occur at 12
172 km depth (Kimura et al., 2012). This transformation is consistent with experimental
173 findings on clays that showed only a minor increase in the coefficient of friction as a
174 function of smectite-to-illite transformation and effective normal stress (i.e. from 0.27

to 0.4) (Saffer et al., 2012). However, there is a significant increase in the friction coefficient associated with a decrease in water content (e.g. by dehydration), or an increase in quartz content in the system (e.g. by silicization and/or precipitation of quartz veins) (Ikari et al., 2007).

2.3 Bi-material fault surface

The subduction interface is on the boundary between the oceanic lithospheric layer and various hanging-wall materials (e.g., wedge and various mantle layers that vary with depth) which can lead to ill-posedness and numerical instability in terms of modelling due to the bi-material propagation (Cochard and Madariaga, 1996). To accommodate for this, the evolution of the normal stress is regularized whereby the frictional strength depends on the evolving normal stress σ_e that, in turn, varies due to normal stress perturbations σ_n depending on either a slip-rate-based or a constant characteristic time scale (Rubin and Ampuero, 2007):

$$\frac{d\sigma_e}{dt} = \frac{\alpha_e|v| + v^*}{\delta_D}(\sigma_n - \sigma_e) \qquad \text{(Eq. 3)}$$

where v^* is a characteristic slip rate, δ_D a characteristic slip scale, $|v|$ is the local value of slip rate, and α_e can assume the values 0 or 1. For this study, $v^* = 0$, $\alpha_e = 1$, and $\delta_D = 0.3\, d_{th}$ were used as they were found to produce numerically stable and physically convergent solutions (Scala et al., 2017). The relationship between the classical slip weakening distance, d_c and the thermal weakening distance, d_{th}, is $d_c \approx 3d_{th}$ (Di Toro et al., 2011).

200 ***2. 4 Presence of fluids***

201 In order to account for the effect of fluids we consider the dynamic Coulomb
202 wedge theory (Wang and Hu, 2006) which proposes that fluid pressure ratio, λ, and
203 effective basal friction, defined as $\mu_b' = \mu(1-\lambda)$ (Wang et al., 2010) where μ is the
204 coefficient of friction, vary between the front, middle and back of the forearc prism.
205 Based on analysis of seismic profiles and thermal models (Kimura et al., 2012), λ =
206 0.9 was applied to the section of the fault at the back of the prism with λ = 0.95 (depth
207 > 14.6 km) for the middle section of the prism (depth range of 9.6 – 14.6 km). For the
208 frontal section of the prism (< 9.6 km), λ = 0.65 was used. Assuming that μ is similar
209 to the static friction coefficient used in our dynamic simulations (i.e., $\mu = \mu_s$) we can
210 compare our initial conditions with other studies. The initial conditions for our
211 numerical model exhibits μ_b' of 0.0875, 0.0125 and 0.025 to 0.07 for the front, middle
212 and back sections of the accretionary wedge which is comparable to observations (i.e.,
213 > 0.08, < 0.03 and 0.03 for the respective sections of the prism) (Kimura et al., 2012)
214 and $\mu_b' = 0.025$ for the whole fault (Gao and Wang, 2014). Using this depth
215 dependent λ, the principal vertical component of stress was estimated as the
216 difference between lithostatic normal load and hydrostatic pore pressure using the
217 principal vertical stress $\sigma_3 = (1-\lambda) g\, \rho\, z$, where g is the gravity, ρ is the density and
218 z is the depth. The fluid retention depth, Z_{FRD}, is the point at which fluid pressure
219 increases at the same rate as the lithostatic gradient (Suppe, 2014). It defines the
220 strength of the fault at depth: the deeper Z_{FRD} is, the stronger the fault becomes, and if
221 all other parameters are similar, the larger the potential stress drop could be during
222 rupture below Z_{FRD}. We assumed Z_{FRD} ~12 km, the point at which the transformation
223 of the frictional parameters from clay-like to rock-like has ended. Therefore, σ_3 tracks
224 the lithostatic gradient below z_{FRD}. The horizontal principal stress, σ_1, was set to 4.05

225 σ_3 (see Section A2 in *Supplementary Material* on discussion on choice for this scaling
226 factor). The effective normal stress on the fault is calculated based on fault geometry
227 relative to the two principal components of stress. The fault strength, that is the stress
228 at which the fault fails, is a function of the static friction coefficient and the effective
229 initial normal stress (black dashed line in Fig. 4a).
230
231 ***2.5 Initial shear stress distribution***
232 As discussed in the introduction, many of the historical thrust earthquakes in
233 the Tohoku region (Fig. 1), can be described with one patch of heterogeneous but
234 concentrated significant slip suggesting that only one major high shear stress
235 "asperity" might have failed at the yield stress in these events. While this may not be
236 always the case, as earthquakes exhibit in general a large variability in the complexity
237 of their slip distributions (e.g. Lorito et al., 2016), a simplified single high stress
238 asperity model is used here, where the initial stress is spatially concentrated in
239 different locations along the fault plane. In reality, the initial shear stress on the fault
240 plane varies both spatially and temporally and is dependent on a number of
241 phenomena such as loading rate, coupling, and historical earthquakes (Nalbant et al.,
242 2013).
243 In order to control the location of the high stress asperity, the initial shear
244 stress distribution was generated by taking the spatial derivative of a 1D
245 heterogeneous slip distribution constructed using a composite source model (Murphy
246 et al., 2016). The location of the high stress asperity is placed randomly on the fault
247 plane for each simulation. The maximum allowable shear stress in the model is
248 defined by the fault strength, meaning that asperities in the crystalline rock material
249 contain higher stress compared with asperities in clay-like material. Nucleation is

250 achieved by lowering the effective normal stress such that the fault strength is a few
251 percent below the initial shear stress (see Fig. S2 in *Supplementary Material* for
252 examples). The location of the nucleation is randomly chosen to be within the asperity
253 on the fault.
254
255 **3. Results**
256 Initially, three separate simulations with asperity locations at different depths
257 were chosen (15 km, 19 km and 36 km) as a case study (Fig. 4a). These three
258 simulations are referred to as "shallow" (blue), "intermediate" (orange) and "deep"
259 (purple) in reference to the relative location of the three asperities. Later this
260 procedure is extended to 45 simulations with asperity locations randomly chosen
261 between 10 - 40 km depth.
262 ***3.1 Breakdown Energy***
263 The three simulations produce radically different slip distributions (Fig. 4b):
264 the deep asperity produced a concentrated patch of slip (maximum slip of 16 m); the
265 intermediate asperity produced the largest earthquake (maximum slip of 38 m) with
266 surface rupture; while the shallow asperity produced the smallest earthquake
267 (maximum slip of 9.5 m). The differences in the amount of slip and earthquake size in
268 our model can be traced back to the depth variation of the fault strength (Fig. 4a) and
269 its evolution with slip (Fig. 4c). This depth dependence in turn plays an important role
270 in controlling the interplay between the release of stored elastic energy and
271 breakdown energy, G_b^i. The breakdown energy G_b^i has been calculated by numerically
272 integrating the evolution of shear stress over the slipping distance using the formula
273 (Abercrombie and Rice, 2005):
274

$$G_b^i = \int_0^{\delta} [\tau(\delta') - \tau(\delta)\,]d\delta' \qquad \text{(Eq .4)}$$

where δ is the total slip. The G_b^i was calculated of each point on the fault where co-seismic slip occurs in the three case studies depicted in Fig 4. The amount of energy required to propagate the rupture dramatically increased below 17 km depth by at least a factor of 50 as shown in Fig. 5a.

3.2 Energy Release Rate

The stress drop, $\Delta\sigma$, systematically increased from 4 MPa to 20 MPa with increasing depth (Fig. 5b). The static stress drop has been calculated using $\Delta\sigma = \tau_o - \tau_f$ where τ_f is the shear stress at the end of rupture and τ_o is the initial shear stress (Kato, 2012). Negative stress drop may occur (as is the case in Fig. 5b) when the stress at a point on the fault is higher at the end of the simulation than at the start. This can occur beyond the arrest region of the earthquake where fault strength does not evolve to residual dynamic strength and therefore the stress in this zone is at a higher level relative to before the earthquake. Negative stress drops may also occur when the initial stress is less than the dynamic strength of the fault ($\tau_o < \mu_d\sigma_n$), in such cases rupture can continue to propagate in these unfavourable zones for a limited distance depending on the energy release rate and G_b^i (Kozdon and Dunham, 2013).

Taking the square of the static stress drop as a proxy for the energy release rate ($G^* \propto \Delta\sigma^2$, assuming rupture velocity remains constant (Nielsen et al., 2016)), this latter quantity increased by a factor of 25 with depth. This depth-dependent relative difference between G_b^i and G^* made it difficult for rupture to propagate out of the trench zone. Therefore, earthquakes that nucleate in shallower clay-rich lithology are more likely to propagate along strike rather than down-dip producing the large

300 length-to-width ratios observed for tsunami earthquakes (e.g., 1896 Meiji (Tanioka
301 and Satake, 1996), 1992 Nicaragua (Ihmlé, 1996), 2006 Java (Ammon et al., 2006)).
302
303 ***3.3 "Shallow" earthquakes***
304 Comparing the deepest and shallowest nucleating earthquakes in Fig. 4a, both
305 have comparable duration (Fig. 6a) and tsunami source amplitude (Fig. 6b and
306 Section A3 in *Supplementary Material*) despite the latter being smaller in size; these
307 findings make the shallowest event in principle compatible with a tsunami earthquake
308 (Grezio et. al., 2017; Satake and Tanioka, 1999). Additional simulations reveal that
309 earthquakes with centroid depth (i.e., the average depth of the slipping area of the
310 earthquake weighted by the slip) located in the high pore pressure zone under the
311 accretionary wedge had consistently longer normalized rupture durations (duration of
312 earthquake has been normalized with respect to moment, see Section A4 in
313 *Supplementary Material*) when compared with earthquakes from other zones on the
314 fault (Fig. 7a). This is a systematic feature in our simulations and it is also consistent
315 with seismological observations (Bilek and Lay, 1999). This depth dependent
316 variation of rupture duration is due to a decrease in both the average stress drop and
317 rigidity (Figs. 7b-c) at shallow depths confirming the hypothesis that rupture duration
318 is linked with depth varying mechanical properties (Bilek and Lay, 1999).
319 Additionally, for earthquakes where significant slip is in the high pore pressure zone
320 the average rupture velocities were in the range of 1.2–2.2 km/s (Fig. 7d). This range
321 is comparable to that estimated for tsunami earthquakes (e.g., 2006 Java M_w 7.8
322 tsunami earthquake which occurred close the Sunda trench and had a rupture velocity
323 range of 1.0 – 1.5 km/s (Ammon et al., 2006)). Hence, the shallow earthquake (blue
324 line in Fig. 4b), with its longer duration, small average stress drop and slow average

rupture velocity, appears to be similar to the 1896 Meiji tsunami earthquake (Tanioka and Satake, 1996) (Fig. 1).

3.4 "Intermediate" depth earthquake

For the intermediate earthquake (orange line and dots, Figs 4-6), nucleation was in a zone where G^* and G_b^i are large (end of the rock to clay transition), but as rupture propagated up-dip the fault became weaker and G_b^i became smaller in the clay-rich material. Additionally, in thrust environments, seismic waves generated at depth by rupture and reflected back onto the fault by the free surface have been shown to induce tensile normal stress perturbations producing larger stress drops and slip near the surface (Nielsen, 1998; Oglesby et al., 1998) as well as promoting rupture in shallow velocity-strengthening environments (Kozdon and Dunham, 2013). This has also been noted in laboratory experiments where velocity strengthening clays at slow slip-rates and low effective normal stresses (< 30 MPa) become velocity weakening (Saffer and Marone, 2003) and have at the same time low G_b^i at slip-rates comparable to those observed during earthquakes (Faulkner et al., 2011). This means that rupture can easily propagate into clay-rich zones even when there is little initial shear stress present in the accretionary wedge.

This easier rupture propagation in clay-rich zones could explain the large size of 2011 Tohoku earthquake which nucleated at 20 – 25 km depth (Chu et al., 2011). In the case study, rupture travelled up-dip into the wedge, with a significant amount of slip occurring above 15 km depth, which is comparable to the slip inversions for the Tohoku earthquake (e.g. Romano et al., 2014, Fig. 1). The seismic moment release rate from the intermediate asperity is much larger and longer than the deepest and shallowest earthquakes (Fig. 6a) and produced the largest tsunami source (Fig. 6b). In

some simulations where the asperity is located at a slightly deeper depth than the intermediate case study, rupture that initially propagates up-dip to the surface then propagated back down the fault again (Fig. 8c), this is a feature that has been suggested for the 2011 M_w 9 earthquake (Ide et al., 2011). Hence, we classify the intermediate simulation as a great thrust earthquake similar to the 2011 M_w 9.0 Tohoku earthquake.

3.5 "Deep" earthquakes

For the deep earthquakes, the distance between the asperity and the clay-rich trench is relevant. This is shown in Fig. 7e, where the earthquakes with the largest seismic moment release had centroid depths between 15 – 20 km. Below a certain depth of ~26 km, the distance from asperity to the clay-rich material was too far relative to the G^* for rupture to reach it; this produced a relatively smaller thrust earthquake (e.g., the 'deep' case study, purple line and dots, in Figs 4-6). These smaller thrust earthquakes had centroid depths below 20 km, had a larger stress drop (Fig. 7b), a faster rupture velocity (Fig. 7d) and larger average G_b^i (Fig. 7f) compared to the great thrust and tsunami earthquakes. They produced only one patch of significant slip making them comparable to the historical M_w 7 – 8 thrust earthquakes in Fig. 1.

4. Discussion

4.1 Varying scaling between principal stresses

Several assumptions were made in the construction of the numerical model. Therefore, a sensitivity study was performed to determine the robustness of the

variation with depth of seismic ruptures features, in response to the initial parameters chosen in the model. For example, in the original set of simulations, the principal components of stress were assumed to have a $\sigma_1 = 4.05\,\sigma_3$. In an additional set of 15 simulations, this was changed to $\sigma_1 = 5.0\,\sigma_3$ to evaluate the effect of different regional principal stresses ratios. The value $\sigma_1 = 5.0\,\sigma_3$ was selected based on previous studies which used ratios of 4.7545 (Ma, 2012) and 5.0 (Brace and Kohlstedt, 1980). Comparing the average moment release, stress drop, G_b^i and rupture velocity per simulation (Fig. S8 in *Supplementary Material*), the change in principal stress ratios has not affected the depth dependent features observed in the original set of simulations.

4.2 Varying the fluid retention depth

Another test was done to examine the effect of altering the fluid retention depth, Z_{FRD}. Two additional sets of simulations (15 in each case) were run where z_{FRD} was shifted ± 5 km from the original depth, i.e. 7 km and 17 km. The effect on yield stress and initial stress distributions, can be viewed in the *Supplementary Material* (i.e. Fig. S4 for the original setup, Fig. S6 for Z_{FRD} = 7 km, and Fig. S7 for Z_{FRD} = 17 km in Section A5). Fig. 9 shows that the earthquakes in the ensemble with Z_{FRD} = 17 km produce more energetic earthquakes (i.e. large moment release and stress drop for intermediate size events). However, the general depth dependent trend observed in the original set of simulations (i.e., Z_{FRD} = 12 km) is still present. This is not the case when Z_{FRD} = 7 km where the depth dependent trends observed in the original study break down with earthquakes at depth exhibiting low rupture velocities (≈ 1 km/s) and long normalised duration. This breakdown in trend is due to the deeper sections of the fault becoming too weak (the yield stress drops below 20 MPa) to store sufficient

400 elastic strain energy relative to the breakdown energy. For Z_{FRD} = 7 km there is still
401 an increase in earthquake moment release at the transition from rock to clay-like
402 material (between 10 - 20 km depth, Fig. 9a) albeit over a reduced scale both in terms
403 of variation in moment and the spatial extent. Therefore, the effect of the rock-clay
404 transition is still present, but as the strength of the deeper section of the fault has
405 become comparable to the near-surface conditions this leads to a breakdown in the
406 original depth-dependent trend.
407
408 ***4.3 Initial stress distributions***
409 While the initial stress distributions used in these simulations were based on a
410 single broad asperity model, in nature, the actual distribution is possibly more
411 complex, and generally unknown. By lowering the initial stress below the residual
412 shear stress outside of the asperity (i.e., $\tau < \mu_d \sigma_n$) rupture propagation was curtailed.
413 Repeating the case studies presented in Fig. 4 with a higher initial stress outside of the
414 asperity (i.e., $\tau = \mu_d \sigma_n$) produced similar slip distributions for the shallowest and
415 deepest earthquakes (see Fig. 10). The intermediate depth earthquake was larger (with
416 >50 m slip) in comparison with the original simulation. This is due to the intermediate
417 earthquake nucleating near the strongest section of the fault which acts as a barrier in
418 the other two cases. To continue to increase the initial shear stress outside of the
419 asperity would ultimately lead to all earthquakes rupturing the full seismogenic zone
420 with very little constraint on nucleation location and/or initial asperity location.
421 Whether sections of the fault contain shear stress lower than the residual shear
422 strength is unknown; phenomena such as dynamic overshoot and low coupling may
423 contribute to it occurring. Alternative phenomena that would cause rupture arrest
424 include increasing fault strength or G_b^i due to change in effective normal stress (i.e.,

425 due to changes in pore pressure/fault geometry) and/or frictional parameters (i.e.,
426 variations in fault material types). Our simplification provided a method for
427 decoupling rupture features at different depths, and despite its limitations revealed
428 itself effective in clarifying significant general relations between frictional properties
429 and rupture dynamics in a subduction environment.

430 A less simplistic initial stress distributions could be achieved, for example, by
431 considering multiple asperities of varying sizes on the fault plane. In such a situation
432 rupture becomes more complex, for example rupture velocity and slip-rate have been
433 shown to be strongly affected by sharp changes in initial shear stress and frictional
434 parameters on the fault plane (Huang et al., 2013). In the simulations presented in this
435 study, rupture velocity generally varies smoothly (see Fig. 8) with the exception being
436 in certain cases when the asperity is located at intermediate depths where the rupture
437 jumps to the very high pore pressure zone (Fig. 8c) due to this section of the fault
438 being very weak. This effect could be negated by considering a highly compliant
439 wedge or off-fault inelastic deformation (as the current numerical model is purely
440 elastic), particularly around the high pore pressure zone, which would slow down the
441 rupture velocity (Lotto et al., 2017; Ma, 2012).

442 Finally, our pre-stress models are not derived from a complete description of a
443 seismic cycle on the analysed fault, since our goal was to understand how depth-
444 dependent frictional behavior may control, to first order, rupture dynamics.

445

446 ***4.4 Along strike variation of frictional parameters***

447 The numerical models presented here are two dimensional and do not account
448 for along strike heterogeneity (i.e. the fault is a line rather than a 2D surface). For
449 example, strong variations in the fluid retention depth along the strike of the fault

450 would lead to along strike variation in fault strength at depth. In our simulations,
451 moving the fluid retention depth up 7 km weakened the fault at depth with the result
452 that great earthquakes were no longer generated at depth (compare blue and black
453 dots in Fig. 9). As demonstrated by the smaller size of earthquakes that nucleated at
454 shallow depths in our ensemble of simulations, it is difficult for rupture to propagate
455 into stronger patches of the fault. Shao et al. (2011) proposed that the repeat M7
456 earthquakes (i.e., 1981 and 2011) occur in relatively weak sections of the fault
457 compared to a potential stronger patch where the 2011 M9 earthquake nucleated. This
458 hypothesis is complementary to our findings whereby along strike variations in the
459 fluid retention depth provides one possible mechanism to explain variations in
460 strength. Other mechanisms such local changes in fault material, fault geometry and
461 pore pressure are other potential means of causing along strike variations in fault
462 strength. On a two-dimensional surface this additional complexity in turn makes
463 rupture propagation more complex as it can conceivably go around barriers while the
464 relative location of surrounding high stress asperities to nucleation can produce
465 rupture directivity (Murphy and Nielsen, 2009). Consequently, while our 2D dynamic
466 model produces depth dependent features similar to seismological observations (Bilek
467 and Lay, 1999), further work involving 3D dynamic rupture simulations would be
468 required to investigate the role of along strike heterogeneity. Particularly in explaining
469 the difference between M7 earthquakes relative to the M9 2011 earthquake given that
470 they nucleate at similar depths.
471
472 ***4.5 Friction Law***
473 With the choice of slip weakening friction law, earthquake rupture was
474 generally crack-like in the simulations (Fig. 8). Friction laws where fault strength

475 evolves with slip rate are more likely to produce pulse-like ruptures (Nielsen and
476 Carlson, 2000; Zheng and Rice, 1998), with shorter rise-time compared to crack-like
477 ruptures. Additionally, velocity-strengthening zones near the surface can further
478 complicate rupture dynamics (Kozdon and Dunham, 2013; Lotto et al., 2017).
479 Consequently, it would be beneficial to perform studies with rate-based friction laws
480 in the future.

481 Ultimately, the aim is to simulate the full seismic cycle with friction laws
482 derived from experiments (and physical fault processes) that are consistent with
483 conditions on the fault during the different stages of the seismic cycle. Nevertheless,
484 despite the simplified framework provided by the single asperity model used here, our
485 model manages to reproduce observed geophysical features between the different
486 subduction zone earthquake types in this mega-thrust environment. The observed
487 differences, can, to first order, be ascribed to rupture dynamics effects coupled with a
488 depth-dependent friction law based that accounts for the expected geology at the
489 Japan Trench.

490

491 ***4.6 Site specific nature of study***

492 Our findings are regional as they are specific to the Tohoku trench
493 environment. A meaningful extrapolation of these results to other subduction zones
494 would require at least similarity in depth dependent frictional properties and fault
495 geometry. For example, in this study, frictional properties based on a clay-like
496 material was chosen as this was observed at Tohoku (Chester et al., 2013). However,
497 soft sediment in the nearby Nankai trench is more sandy in nature (Hirono et al.,
498 2014). Dynamic simulations comparing the two environments have shown that a more
499 sandy sediment produces a larger thermal pressurisation during dynamic rupture but

this is offset by higher initial excess fluid pressure (Hirono et al., 2016). Consequently, care must be taken in applying the finds from one subduction zone to another.

5. Conclusion

In nature, subduction zone faults are more complicated than what is depicted in our numerical models (fault roughness, multiple asperities, off-fault inelastic deformation etc.). In particular, our choice of type of initial stress distribution (i.e. an 'asperity' model) only examines a small part of the potential stress models and it might not be compatible with stress profiles derived from the modelling of the whole seismic cycle. Therefore, future work should focus on the application of the model to a much wider range of heterogeneous initial stress conditions.

Nevertheless, our model based on lithological and depth dependent friction law tuned to the 2011 Tohoku fault region allows us to better understand and reproduce to the first order the different types of (tsunamigenic) earthquakes. Consistently with geophysical observations, the numerical simulations have shown that events with a number of characteristics resembling tsunami earthquakes were generated either near to or below the accretionary wedge. Their rupture area was constrained to remain there due to the fault strength and breakdown energy increasing with depth. We also found that standard thrust earthquakes, with relatively larger stress drops, shorter durations and faster rupture velocities occurred in crystalline rock where both the energy release rate and fault resistance are high. Finally, if the rupture initiated at the bottom of or just below the rock-clay transition and propagated towards the surface and into a zone characterised by low fault strength and frictional resistance, this leads to the production of great thrust earthquakes.

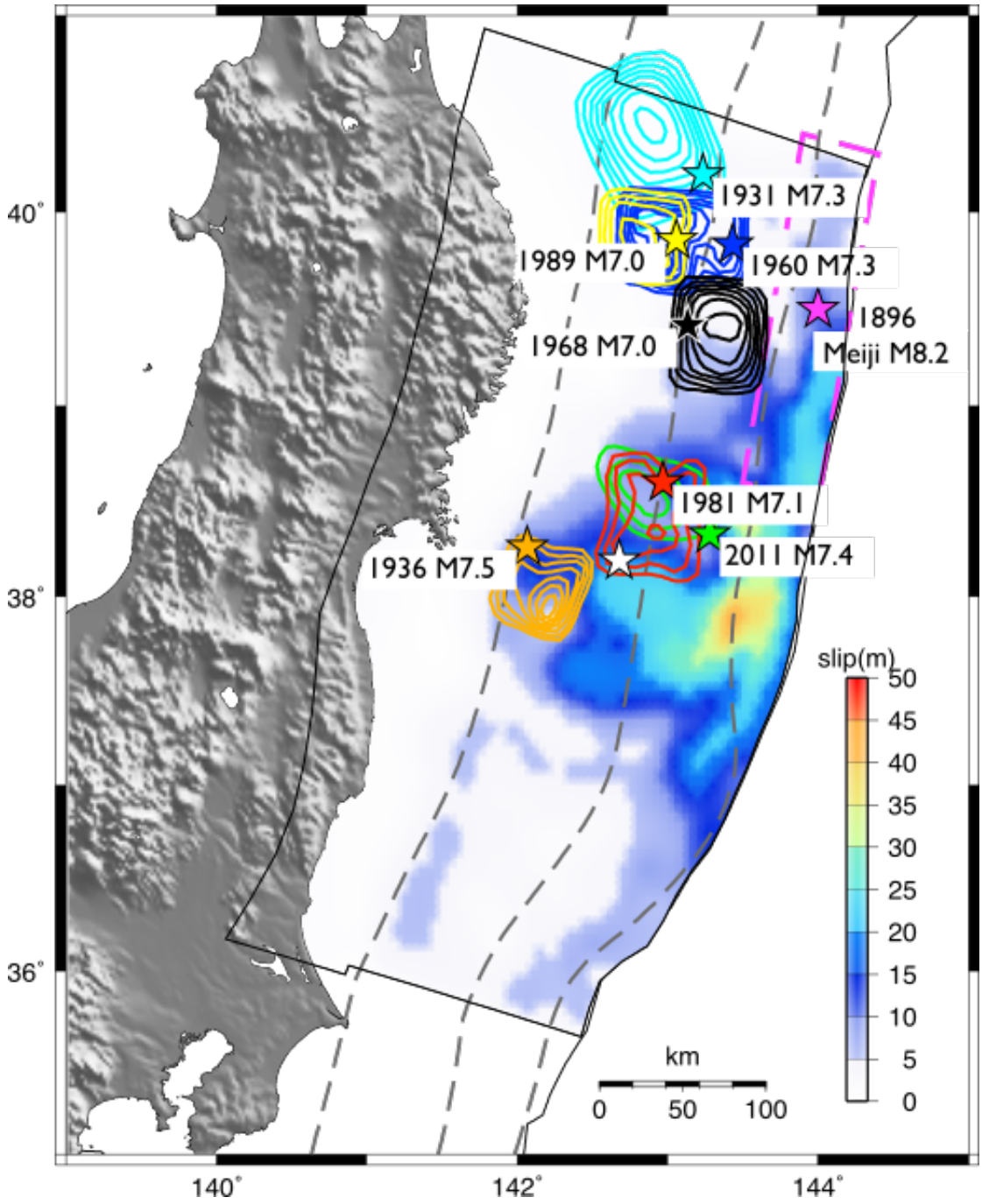

Figure 1: Earthquake history off the Pacific coast of Tohoku region and model setup. Coloured contours represent slip distributions at 0.5 m interval for a number of

historical thrust earthquakes(Shao et al., 2011; Yamanaka and Kikuchi, 2004); The magenta dashed box represents the location for the 1896 Meiji tsunami earthquakes (M 8.2-8.4). The colour slip distribution is the M_w 9 Tohoku earthquake(Romano et al., 2014), the red star is its epicentre. Dashed grey line is depth at 10, 20 and 40 km.

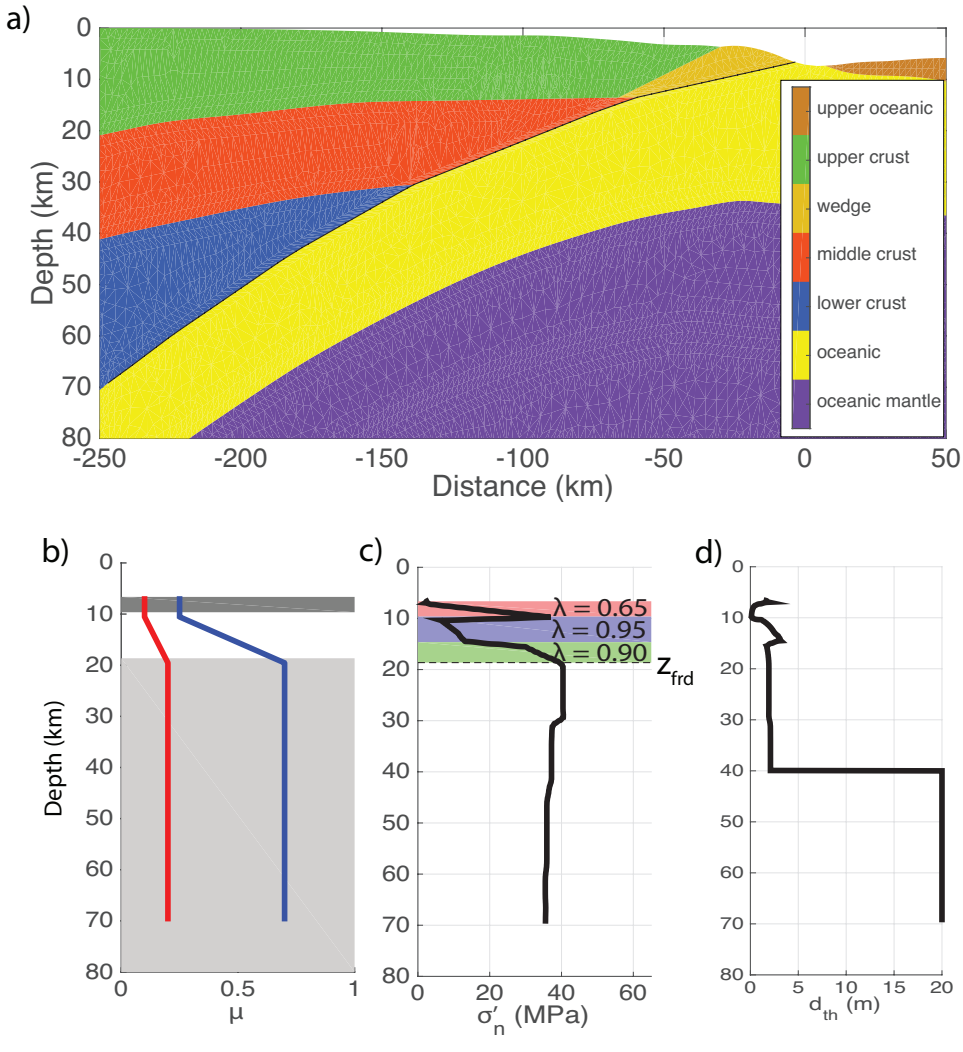

Figure 2: Numerical model set up. **a)** structural model used in the numerical simulations, black line denotes the subduction interface. **b)** variation of frictional coefficients with depth: the dark and light grey boxes denote the clay-rich and crystalline rock frictional coefficients; the white is the transition between the two

materials. Solid blue and red lines are the static and dynamic coseismic coefficients of friction respectively. **c)** the variation of the effective normal stress with depth, coloured boxes denote different pore fluid to overburden stress ratio, λ. The dashed black line denotes the fluid retention depth. **d)** variance of d_{th} with depth which is a function of effective normal stress and frictional material type (i.e., rock or clay-rich).

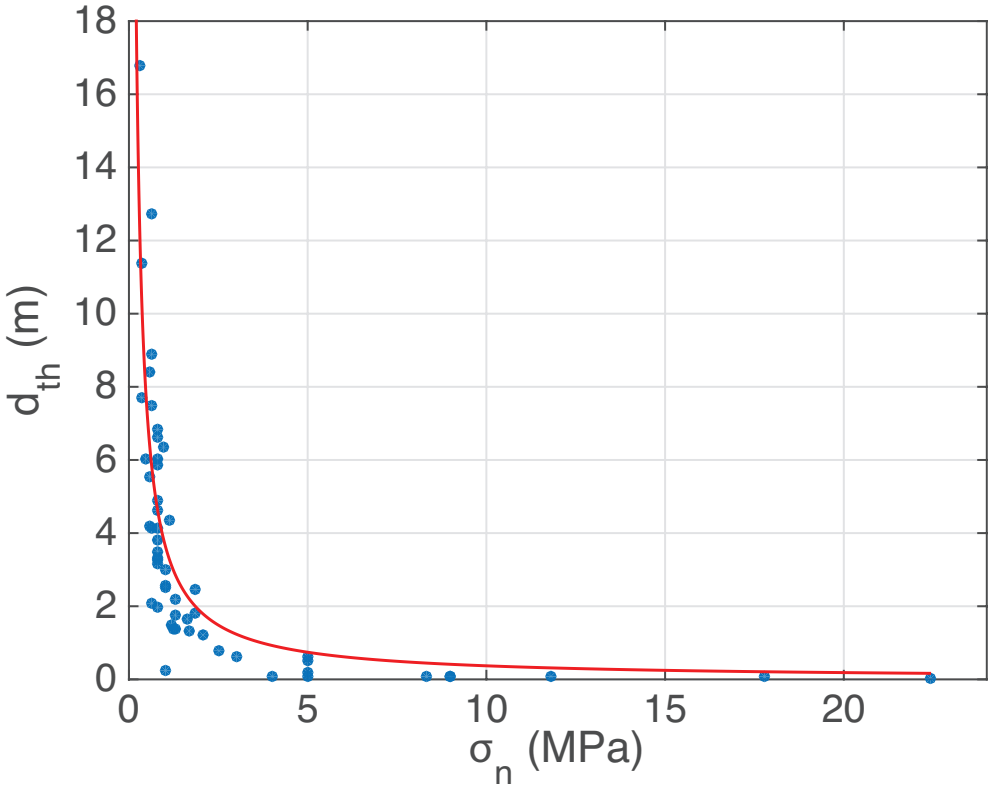

Figure 3: The fit of $d_{th} = 3.712\ \|\sigma_n\|^{-1}$ (red line) compared with the laboratory experiments performed on clay material (see Table S5 in *Supplementary Material* for references).

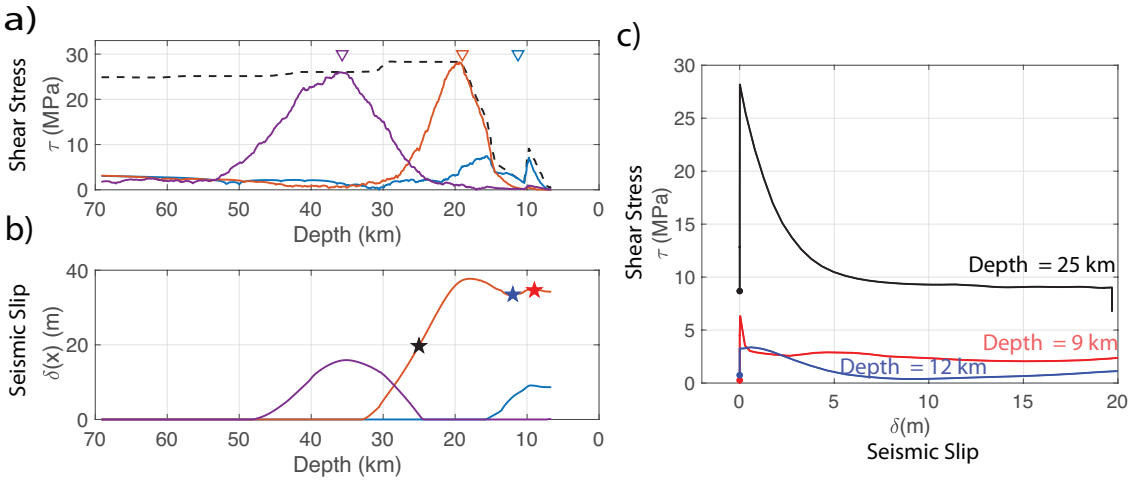

556

557 **Figure 4:** Modelled environment earthquake source parameters **a)** The different solid
558 colours relate to the initial shear stress distributions used in the three simulations
559 which reproduce a tsunamigenic great thrust earthquake (orange), tsunami earthquake
560 (blue) and thrust earthquakes (purple). The same colour code is used for all subplots.
561 Triangles are nucleation locations. Black dashed line is the fault strength. **b)** Slip
562 distributions resulting from simulations where the colours relate to the initial stress
563 distributions in a). **c)** Shear stress evolution with slip at three different depths (25 km
564 black line, 12 km blue line, 9 km red line) taken from intermediate simulation (i.e.,
565 orange line in b). The locations are also highlighted by stars in subplot b) where a
566 similar colour scale has been used. Dots denote the initial stress at each location.

567

568

569

570

571

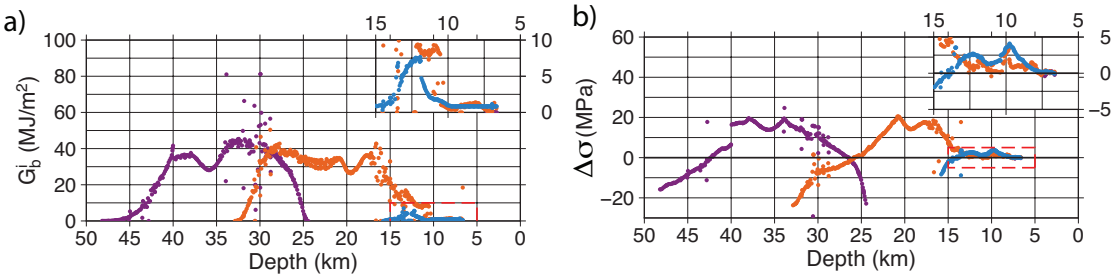

572

573 **Figure 5: a)** Breakdown energy calculated at each point along the fault. Insets are

574 expansions of the data inside the red dashed boxes. **b)** Static stress drop calculated at

575 each point along the fault.

576

577

578

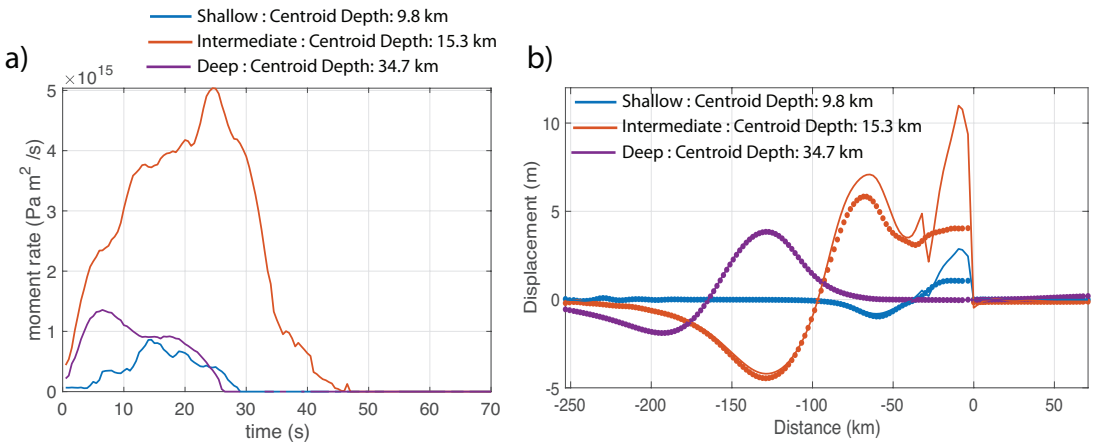

579

580 **Figure 6: a)** Moment release rate with time. **b)** Vertical seafloor displacement (dotted

581 lines) and estimated tsunami source (solid lines, details in Section A3 in

582 *Supplementary Information*). Horizontal distance as in Fig. 2 where 0 km indicates the

583 point where the fault reaches the seafloor.

584

585

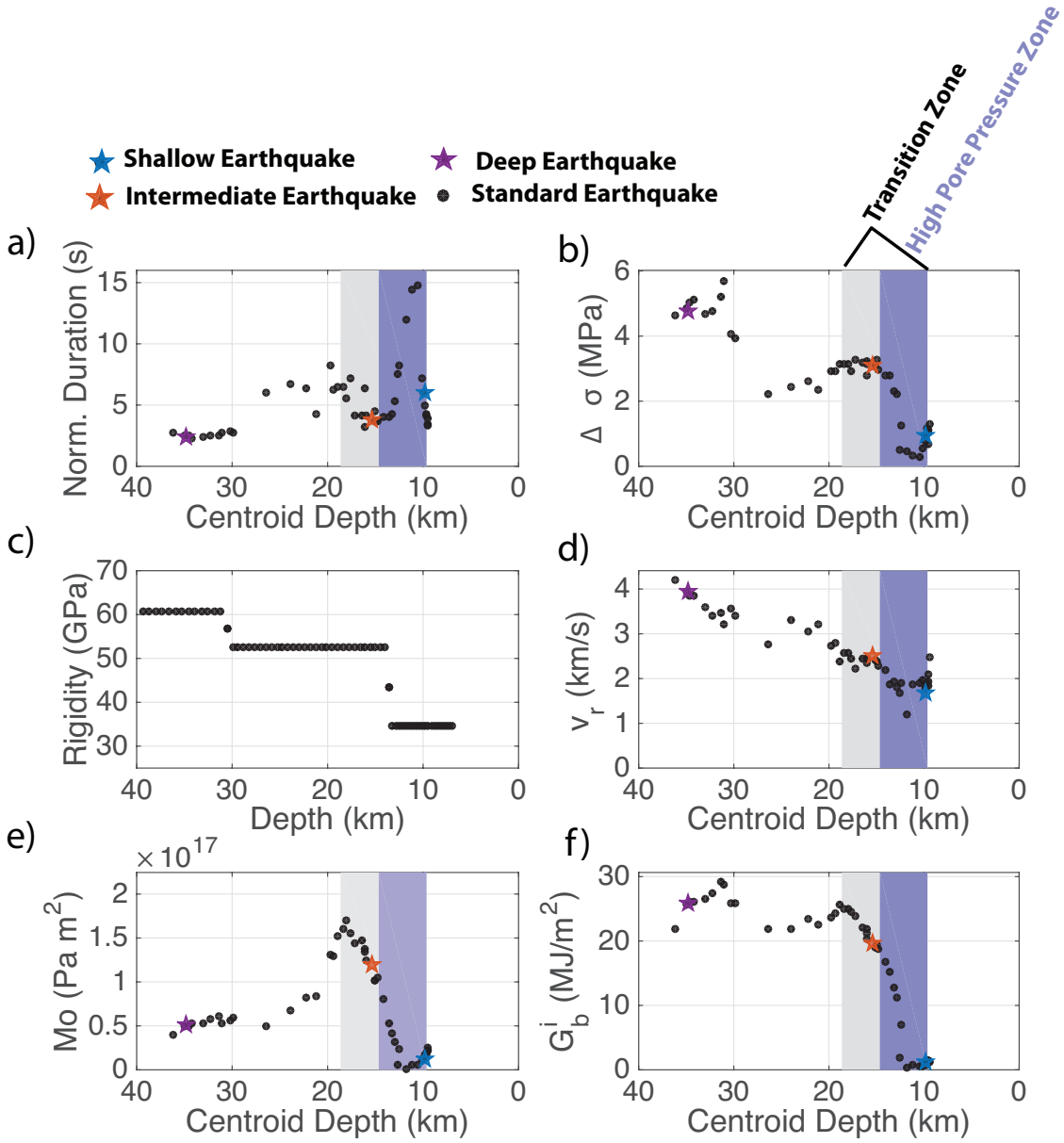

586

587 **Figure 7:** Rupture parameters plotted against centroid depth for a number of
588 simulations where only the location of the high stress asperity varies with depth. The
589 purple box is the zone with very high pore pressure ($\lambda = 0.95$); grey and purple boxes
590 together demark the transition zone between clay-like and crystalline rock frictional
591 parameters. **a)** Normalised earthquake duration; **b)** Average static stress drop; **c)** shear
592 modulus averaged across the fault plane to account of bi-material wall rocks; **d)**
593 Average rupture velocity; **e)** Moment of the (1D) simulated earthquakes (details in

Section A4 in *Supplementary Material*); and **f)** Average breakdown energy. The stars indicate the three case studies presented in Fig. 2 with the same colour code applied.

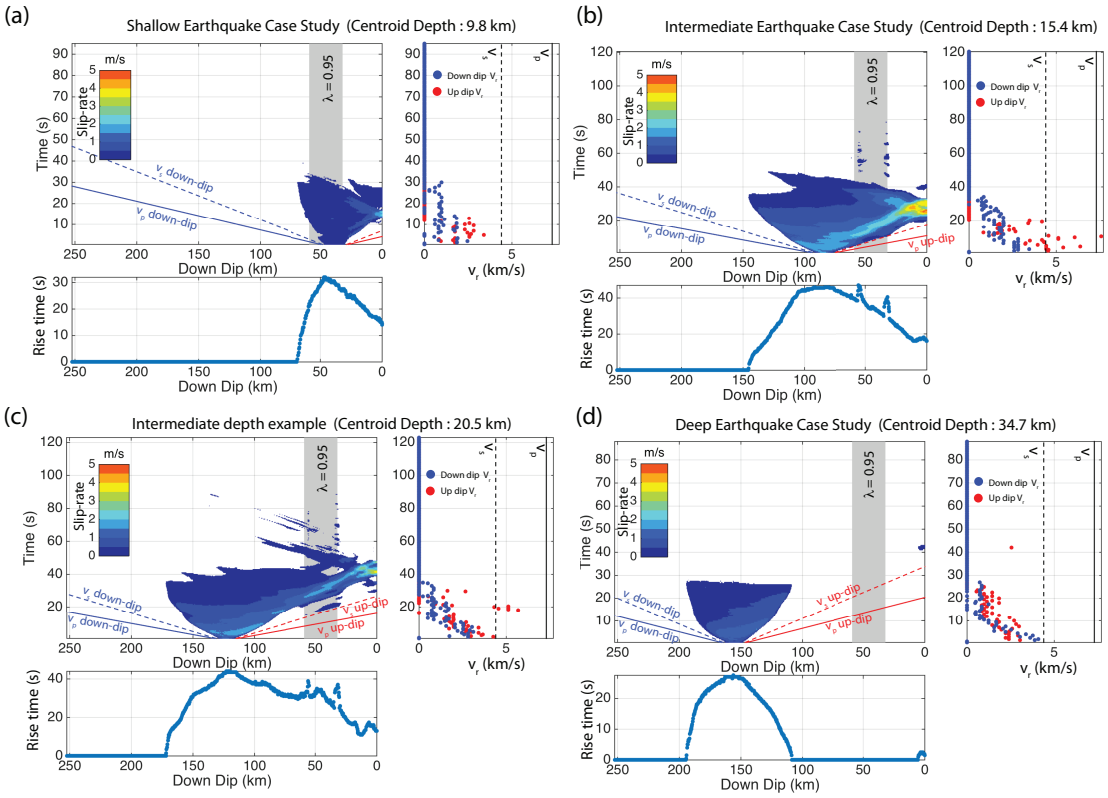

Figure 8: Slip-rate, rupture velocity and rise-time observed in four simulations with increasing fault down-dip location of the asperity (40, 80, 120 and 160 km depth, respectively). These depths correspond to the hypocentral depths of the three cases presented in Fig. 2 and an additional great thrust earthquake which generated a down-dip travelling rupture pulse. In all subplots the solid and dashed lines are the P- and S-wave velocities in the oceanic material (i.e., yellow layer in Fig. 1) with the colour of the line indicating rupture direction (i.e. blue is to the left of the nucleation zone or down-dip, red is the right or up-dip). The light grey box behind the slip-rates defines the zone of very high pore pressure (i.e., $\lambda = 0.95$) in the wedge. **a)** Asperity in the

wedge which corresponds to the shallow case study (blue line and dots in Figs. 2 and 3) **b)** Asperity at 20 km depth related to the intermediate case study (i.e., orange data in Figs. 2 and 3). **c)** Asperity at 27 km depth, an example of a great thrust earthquake with a down-dip travelling rupture pulse that was referred to in Section 3.4 **d)** Deep case study (i.e., 39 km) purple colour in Figs. 2 and 3.

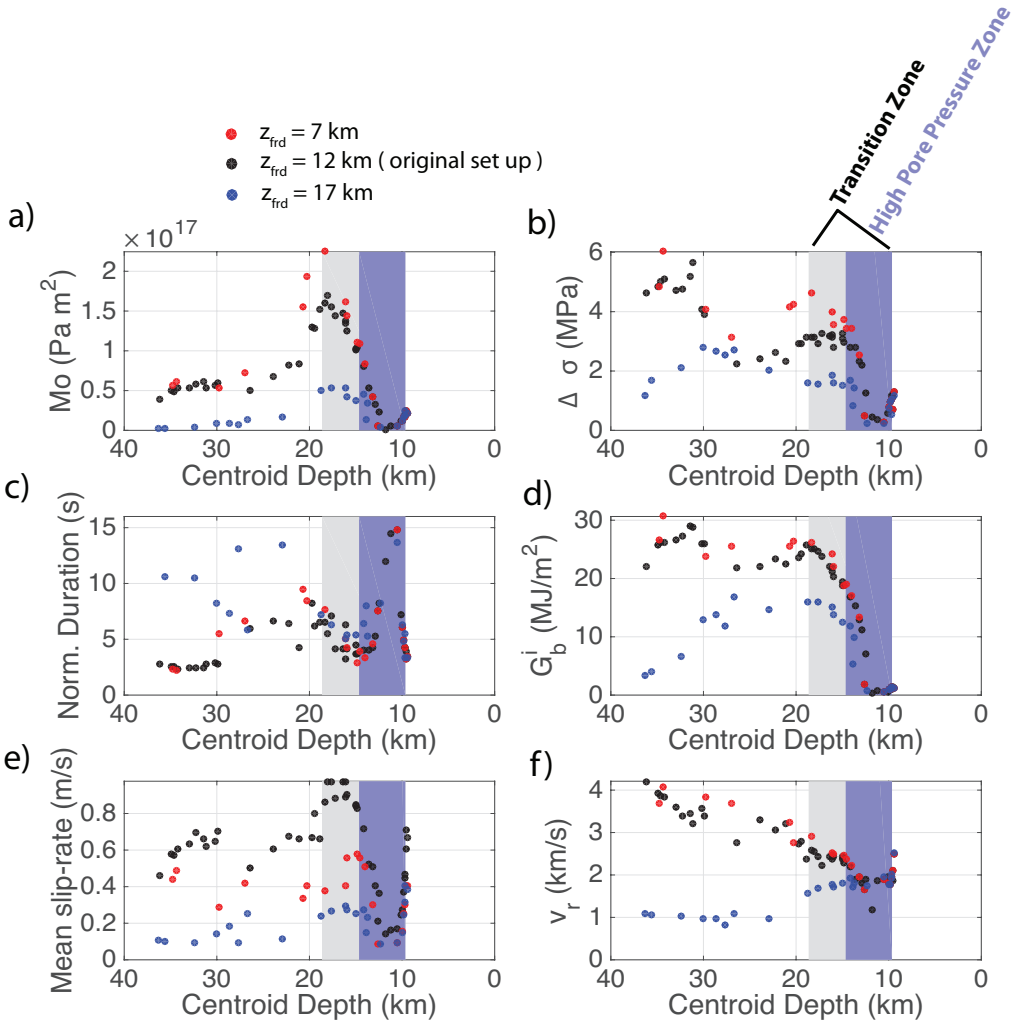

Figure 9: Sensitivity study on varying the fluid retention depth. The black dots are from simulations using the original model discussed in Section 3 (i.e., z_{FRD} = 12 km)

with 45 simulations, the blue dots are the case z_{FRD} = 7 km (15 simulations) and the red dots are case with z_{FRD} = 17 km (15 simulations). **a)** Seismic moment of the simulated earthquake; a constant shear modulus G = 30 GPa rather than a depth dependent shear modulus was used in the calculation as it is commonly used in observational seismology, **b)** Average static stress drop, **c)** average normalised rupture duration, **d)** average breakdown energy, **e)** average slip-rate per earthquake and **f)** average rupture velocity.

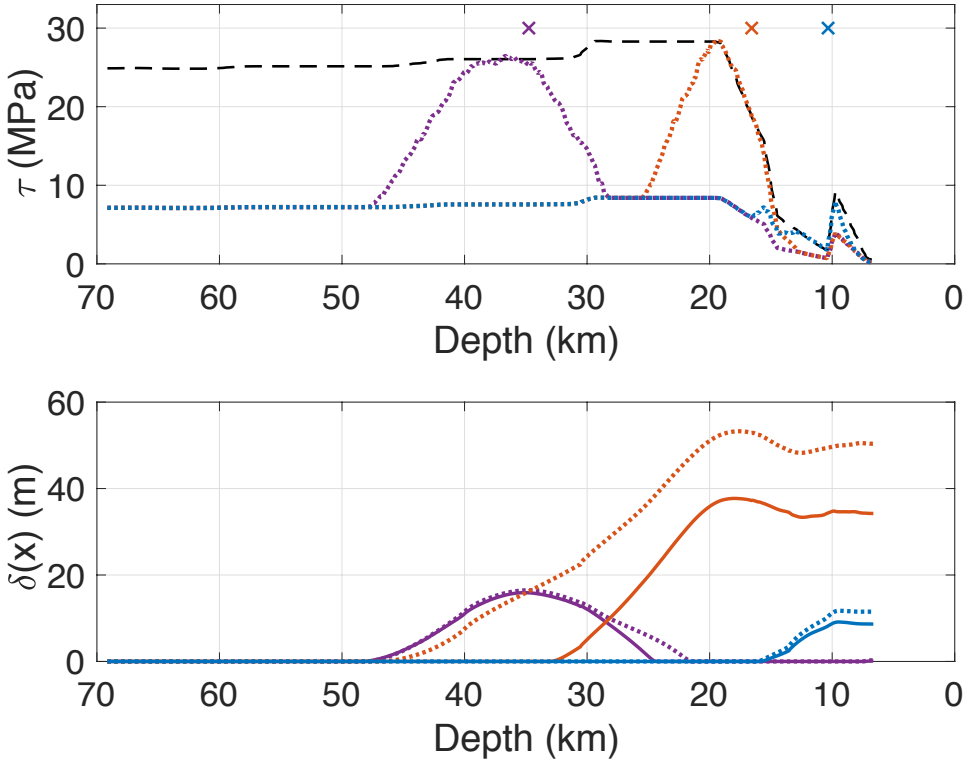

Figure 10: Testing increased background initial stress outside of the asperity. **a)** The black dashed line is the yield strength. The dotted colour lines represent the initial shear stress where stress does not drop below the residual shear stress (i.e. $\tau = \mu_d \sigma_n$). The x's are the nucleation locations for the new (i.e. dashed) set of simulations. **b)** the final slip distributions for each simulation where the colour and line type convention

is same as the one used in subplot a) The solid lines are the slip distributions using the original initial stress distribution (see Fig. 4).

References

Abercrombie, R., Rice, J., 2005. Can observations of earthquakes scaling constrain slip weakening. Geophys. J. Int. 162, 406–424. doi:10.1111/j.1365-246X.2005.02579.x

Ammon, C.J., Kanamori, H., Lay, T., Velasco, A.A., 2006. The 17 July 2006 Java tsunami earthquake. Geophys. Res. Lett 33, L24308–5. doi:10.1029/2006GL028005

Bilek, S.L., Lay, T., 1999. Rigidity variations with depth along interplate megathrust faults in subduction zones. Nature 400, 443–446. doi:10.1038/22739

Bilek, S.L., Rotman, H.M.M., Phillips, W.S., 2016. Low stress drop earthquakes in the rupture zone of the 1992 Nicaragua tsunami earthquake. Geophys. Res. Lett 43, 10,180–10,188. doi:10.1002/2016GL070409

Brace, W.F., Kohlstedt, D.L., 1980. Limits on lithospheric stress imposed by laboratory experiments. J. Geophys. Res. 85, 6248–6252. doi:10.1029/JB085iB11p06248

Chester, F.M., Rowe, C., Ujiie, K., Kirkpatrick, J., Regalla, C., Remitti, F., Moore, J.C., Toy, V., Wolfson-Schwehr, M., Bose, S., Kameda, J., Mori, J.J., Brodsky, E.E., Eguchi, N., Toczko, S., Expedition 343 and 343T Scientists, 2013. Structure and Composition of the Plate-Boundary Slip Zone for the 2011 Tohoku-Oki Earthquake. Science 342, 1208–1211. doi:10.1126/science.1243719

Chu, R., Wei, S., Helmberger, D.V., Zhan, Z., Zhu, L., Kanamori, H., 2011. Initiation of the great Mw 9.0 Tohoku–Oki earthquake. Earth Planet. Sci. Lett. 308, 277–283. doi:10.1016/j.epsl.2011.06.031

Cochard, A., Madariaga, R., 1996. Complexity of seismicity due to highly rate-dependent friction. J. Geophys. Res. 101, 25,321–25,336.

Cubas, N., Lapusta, N., Avouac, J.-P., Perfettini, H., 2015. Numerical modeling of long-term earthquake sequences on the NE Japan megathrust: Comparison with observations and implications for fault friction. Earth Planet. Sci. Lett. 419, 187–198. doi:10.1016/j.epsl.2015.03.002

Del Gaudio, P., Di Toro, G., Han, R., Hirose, T., Nielsen, S., Shimamoto, T., Cavallo, A., 2009. Frictional melting of peridotite and seismic slip. J. Geophys. Res. 114, B06306–19. doi:10.1029/2008JB005990

Di Toro, G., Han, R., Hirose, T., De Paola, N., Nielsen, S., Mizoguchi, K., Ferri, F., Cocco, M., Shimamoto, T., 2011. Fault lubrication during earthquakes. Nature 471, 494–498. doi:10.1038/nature09838

Dieterich, J., 1979. Modeling of Rock Friciton: 1. Experimental results and constituive equations. J. Geophys. Res. 84, 2161–2168.

Faulkner, D.R., Mitchell, T.M., Behnsen, J., Hirose, T., Shimamoto, T., 2011. Stuck in the mud? Earthquake nucleation and propagation through accretionary forearcs. Geophys. Res. Lett 38. doi:10.1029/2011GL048552

Festa, G., Vilotte, J.-P., 2005. The Newmark scheme as velocity–stress time-

staggering: an efficient PML implementation for spectral element simulations of elastodynamics. Geophys. J. Int. 161, 789–812. doi:10.1111/j.1365-246X.2005.02601.x

Festa, G., and J.-P. Vilotte 2006, Influence of the rupture initiation on the intersonic transition: Crack-like versus pulse-like modes, Geophys. Res. Lett,, 33 (L15320), doi:http://dx.doi.org/10.1029/2006GL026378.

Freed, A., 2005. Earthquake triggering by static, dynamic, and postseismic stress transfer. Annu. Rev. Earth Planet Sci. 33, 335–367. doi:http://dx.doi.org/10.1146/annurev.earth.33.092203.122505

Gao, X., Wang, K., 2014. Strength of stick-slip and creeping subduction megathrusts from heat flow observations. Science 345, 1038–1041. doi:10.1126/science.1255487

Geist, E.L., Bilek, S.L., 2001. Effect of depth-dependent shear modulus on tsunami generation along subduction zones. Geophys. Res. Lett 28, 1315–1318. doi:10.1029/2000GL012385

Grezio, A., Babeyko, A., Baptista, M. A., Behrens, J., Costa, A., Davies, G., Geist, E. L., Glimsdal, S., González, F. I., Griffin, J., Harbitz, C. B., LeVeque, R. J., Lorito, S., Løvholt, F., Omira, R., Mueller, C., Paris, R., Parsons, T., Polet, J., Power, W., Selva, J., Sørensen M., B., Thio, H. K. 2017. Probabilistic Tsunami Hazard Analysis: Multiple sources and global applications. Reviews of Geophysics, 55. doi: 10.1002/2017RG000579

Hacker, B.R., Abers, G.A., Peacock, S.M., 2003a. Subduction factory 1. Theoretical mineralogy, densities, seismic wave speeds, and H2O contents. J Geophys Res 108, 1–26. doi:10.1029/2001JB001127

Hacker, B.R., Peacock, S.M., Abers, G.A., Holloway, S.D., 2003b. Subduction factory 2. Are intermediate-depth earthquakes in subducting slabs linked to metamorphic dehydration reactions? J. Geophys. Res. 108, 1–20. doi:10.1029/2001JB001129

Hartog, den, S.A.M., Niemeijer, A.R., Spiers, C.J., 2012. New constraints on megathrust slip stability under subduction zone P–T conditions. Earth and Planetary Science Letters 353-354, 240–252. doi:10.1016/j.epsl.2012.08.022

Hayes, G.P., Wald, D.J., Johnson, R.L., 2012. Slab1.0: A three-dimensional model of global subduction zone geometries. J. Geophys. Res. 117, B01302–15. doi:10.1029/2011JB008524

Hirono, T., Ishikawa, T., Masumoto, H., Kameda, J., Yabuta, H., Mukoyoshi, H., 2014. Re-evaluation of frictional heat recorded in the dark gouge of the shallow part of a megasplay fault at the Nankai Trough. Tectonophysics 626, 157–169. doi:10.1016/j.tecto.2014.04.020

Hirono, T., Tsuda, K., Tanikawa, W., Ampuero, J.-P., Shibazaki, B., Kinoshita, M., Mori, J.J., 2016. Near-trench slip potential of megaquakes evaluated from fault properties and conditions. Sci. Rep. 1–13. doi:10.1038/srep28184

Huang, Y., Ampuero, J.-P., Kanamori, H., 2013. Slip-Weakening Models of the 2011 Tohoku-Oki Earthquake and Constraints on Stress Drop and Fracture Energy. Pure Appl. Geophys. 171, 2555–2568. doi:10.1007/s00024-013-0718-2

Hyndman, R., Yamano, M., Oleskevich, D., 1997. The seismogenic zone of subduction thrust faults. The Island Arc 6, 244–260.

Ida, Y., 1972. Cohesive Force across the Tip of a Longitudinal-Shear Crack and Griffith's Specific Surface Energy. J. Geophys. Res. 77, 3796–3805.

Ide, S., Baltay, A., Beroza, G.C., 2011. Shallow Dynamic Overshoot and Energetic Deep Rupture in the 2011 Mw 9.0 Tohoku-Oki Earthquake. Science 332, 1426–

729 1429. doi:10.1126/science.1207020
730 Ihmlé, P.F., 1996. Monte Carlo slip inversion in the frequency domain: : Application
731 to the 1992 Nicaragua Slow Earthquake. Geophys. Res. Lett 23, 913–916.
732 doi:10.1029/96GL00872
733 Ikari, M.J., Saffer, D.M., Marone, C., 2007. Effect of hydration state on the frictional
734 properties of montmorillonite-based fault gouge. J. Geophys. Res. 112, B06423–
735 12. doi:10.1029/2006JB004748
736 Kanamori, H., 1972. Mechanism of tsunami earthquakes. Phys. Earth Planet. In. 6,
737 346–359. doi:10.1016/0031-9201(72)90058-1
738 Kato, N., 2012. Dependence of earthquake stress drop on critical slip-weakening
739 distance. J Geophys Res 117. doi:10.1029/2011JB008359
740 Kimura, G., Hina, S., Hamada, Y., Kameda, J., Tsuji, T., Kinoshita, M., Yamaguchi,
741 A., 2012. Runaway slip to the trench due to rupture of highly pressurized
742 megathrust beneath the middle trench slope: The tsunamigenesis of the 2011
743 Tohoku earthquake off the east coast of northern Japan. Earth Planet. Sci. Lett.
744 339-340, 32–45. doi:10.1016/j.epsl.2012.04.002
745 Kozdon, J.E., Dunham, E.M., 2014. Constraining shallow slip and tsunami excitation
746 in megathrust ruptures using seismic and ocean acoustic waves recorded on
747 ocean-bottom sensor networks. Earth Planet. Sci. Lett. 396, 56–65.
748 doi:10.1016/j.epsl.2014.04.001
749 Kozdon, J.E., Dunham, E.M., 2013. Rupture to the Trench: Dynamic Rupture
750 Simulations of the 11 March 2011 Tohoku Earthquake. B. Seismol. Soc. Am.
751 103, 1275–1289. doi:10.1785/0120120136
752 Lay, T., Kanamori, H., Ammon, C.J., Koper, K.D., Hutko, A.R., Ye, L., Yue, H.,
753 Rushing, T.M., 2012. Depth-varying rupture properties of subduction zone
754 megathrust faults. J. Geophys. Res. 117, B04311–21. doi:10.1029/2011JB009133
755 Lorito, S., Romano, F., & Lay, T., 2016. Tsunamigenic earthquakes (2004–2013):
756 Source processes from data inversion. In R. Meyers (Ed.), *Encyclopedia of*
757 *complexity and systems science.* New York: Springer Science+Business Media
758 New York 2015. doi: 10.1007/978-3-642-27737-5641-1
759 Lotto, G.C., Dunham, E.M., Jeppson, T.N., Tobin, H.J., 2017. The effect of compliant
760 prisms on subduction zone earthquakes and tsunamis. Earth Planet. Sci. Lett. 458,
761 213–222. doi:10.1016/j.epsl.2016.10.050
762 Ma, S., 2012. A self-consistent mechanism for slow dynamic deformation and
763 tsunami generation for earthquakes in the shallow subduction zone. Geophys.
764 Res. Lett 39, n/a–n/a. doi:10.1029/2012GL051854
765 Meneghini, F., Di Toro, G., Rowe, C.D., Moore, J.C., Tsutsumi, A., Yamaguchi, A.,
766 2010. Record of mega-earthquakes in subduction thrusts: The black fault rocks of
767 Pasagshak Point (Kodiak Island, Alaska). Geol. Soc. Am. Bull. 122, 1280–1297.
768 doi:10.1130/B30049.1
769 Mitsui, Y., Yagi, Y., 2013. An interpretation of tsunami earthquake based on a simple
770 dynamic model: Failure of shallow megathrust earthquake. Geophys. Res. Lett
771 40, 1523–1527. doi:10.1002/grl.50266
772 Miura, S., Takahashi, N., Nakanishi, A., Tsuru, T., Kodaira, S., Kaneda, Y., 2005.
773 Structural characteristics off Miyagi forearc region, the Japan Trench seismogenic
774 zone, deduced from a wide-angle reflection and refraction study. Tectonophysics
775 407, 165–188. doi:10.1016/j.tecto.2005.08.001
776 Murphy, S., Nielsen, S., 2009. Estimating earthquake magnitude with early arrivals: A
777 test using dynamic and kinematic models. B. Seismol. Soc. Am. 99, No. 1, 1–23.
778 doi:http://dx.doi.org/10.1785/0120070246

779 Murphy, S., Scala, A., Herrero, A., Lorito, S., Festa, G., Trasatti, E., Tonini, R.,
780 Romano, F., Molinari, I., Nielsen, S., 2016. Shallow slip amplification and
781 enhanced tsunami hazard unravelled by dynamic simulations of mega-thrust
782 earthquakes. Sci. Rep. 1–12. doi:10.1038/srep35007
783 Nalbant, S., McCloskey, J., Steacy, S., NicBhloscaidh, M., Murphy, S., 2013.
784 Interseismic coupling, stress evolution, and earthquake slip on the Sunda
785 megathrust. Geophys. Res. Lett 40, 4204–4208. doi:10.1002/grl.50776
786 Nielsen, S., Carlson, J., 2000. Rupture Pulse Characterization: Self-Healing, Self-
787 Similar, Expanding Solutions in a Continuum Model of Fault Dynamic. B.
788 Seismol. Soc. Am. 90, No. 6, 1480–1497.
789 Nielsen, S., Mosca, P., Giberti, G., Di Toro, G., Hirose, T., Shimamoto, T., 2010. On
790 the transient behavior of frictional melt during seismic slip. J. Geophys. Res. 115,
791 B10301–17. doi:10.1029/2009JB007020
792 Nielsen, S., Spagnuolo, E., Violay, M., Smith, S., Toro, G., Bistacchi, A., 2016. G:
793 Fracture energy, friction and dissipation in earthquakes. J. Seismol. 1–19.
794 doi:10.1007/s10950-016-9560-1
795 Nielsen, S.B., 1998. Free surface effects on the propagation of dynamic rupture.
796 Geophys. Res. Lett. 25, 125–128.
797 Niemeijer, A., Di Toro, G., Nielsen, S., Di Felice, F., 2011. Frictional melting of
798 gabbro under extreme experimental conditions of normal stress, acceleration, and
799 sliding velocity. J. Geophys. Res. 116. doi:10.1029/2010JB008181
800 Noda, H., Lapusta, N., 2013. Stable creeping fault segments can become destructive
801 as a result of dynamic weakening. Nature 493, 518–521. doi:10.1038/nature11703
802 Oglesby, D., Archuleta, R., Nielsen, S., 1998. Earthquakes on Dipping Faults: The
803 Effects of Broken Symmetry. Science 280, 1055–1059.
804 doi:http://dx.doi.org/10.1126/science.280.5366.1055
805 Ozawa, S., Nishimura, T., Suito, H., Kobayashi, T., Tobita, M., Imakiire, T., 2011.
806 Coseismic and postseismic slip of the 2011 magnitude-9 Tohoku-Oki earthquake.
807 Nature 475, 373–376. doi:10.1038/nature10227
808 Proctor, B.P., Mitchell, T.M., Hirth, G., Goldsby, D., Zorzi, F., Platt, J.D., Di Toro,
809 G., 2014. Dynamic weakening of serpentinite gouges and bare surfaces at seismic
810 slip rates. J. Geophys. Res. 119, 8107–8131. doi:10.1002/2014JB011057
811 Remitti, F., Smith, S.A.F., Mittempergher, S., Gualtieri, A.F., Di Toro, G., 2015.
812 Frictional properties of fault zone gouges from the J-FAST drilling project (M
813 w9.0 2011 Tohoku-Oki earthquake). Geophys. Res. Lett 42, 2691–2699.
814 doi:10.1002/2015GL063507
815 Romano, F., Trasatti, E., Lorito, S., Piromallo, C., Piatanesi, A., Ito, Y., Zhao, D.,
816 Hirata, K., Lanucara, P., Cocco, M., 2014. Structural control on the Tohoku
817 earthquake rupture process investigated by 3D FEM, tsunami and geodetic data.
818 Sci. Rep. 4. doi:10.1038/srep05631
819 Rubin, A.M., Ampuero, J.-P., 2007. Aftershock asymmetry on a bimaterial interface.
820 Journal of Geophysical Research 112, B05307–23. doi:10.1029/2006JB004337
821 Ruina, A., 1983. Slip instablity and state variable friction law. J. Geophys. Res. 88,
822 10359–10370.
823 Saffer, D.M., Lockner, D.A., McKiernan, A., 2012. Effects of smectite to illite
824 transformation on the frictional strength and sliding stability of intact marine
825 mudstones. Geophys. Res. Lett. 39, L11304. doi:10.1029/2012GL051761
826 Saffer, D.M., Marone, C., 2003. Comparison of smectite- and illite-rich gouge
827 frictional properties: application to the updip limit of the seismogenic zone along
828 subduction megathrusts. Earth Planet. Sci. Lett. 215, 219–235.

doi:10.1016/S0012-821X(03)00424-2
Satake, K., Tanioka, Y., 1999. Sources of Tsunami and Tsunamigenic Earthquakes in Subduction Zones, in: Seismogenic and Tsunamigenic Processes in Shallow Subduction Zones. Pure Appl. Geophys. 154, 467–483. doi:10.1007/978-3-0348-8679-6_5
Sawai, M., Hirose, T., Kameda, J., 2014. Frictional properties of incoming pelagic sediments at the Japan Trench: implications for large slip at a shallow plate boundary during the 2011 Tohoku earthquake. Earth, Planets Space 66, 65. doi:10.1186/1880-5981-66-65
Scala, A., Festa, G., Vilotte, J.-P., 2017. Rupture dynamics along bimaterial interfaces: a parametric study of the shear-normal traction coupling. Geophys. J. Int. 209, 1. doi:10.1093/gji/ggw489
Shao, G., Ji, C., Zhao, D., 2011. Rupture process of the 9 March, 2011 Mw 7.4 Sanriku-Oki, Japan earthquake constrained by jointly inverting teleseismic waveforms, strong motion data and GPS observations. Geophys. Res. Lett. 38, L00G20. doi:10.1029/2011GL049164
Shibazaki, B., Matsuzawa, T., Tsutsumi, A., 2011. 3D modeling of the cycle of a great Tohoku-Oki earthquake, considering frictional behavior at low to high slip velocities. Gephys. Res. Lett. 38, L21305. doi: 10.1029/2011GL049308
Suppe, J., 2014. Fluid overpressures and strength of the sedimentary upper crust. J. Struct. Geol. 69, 481-492. doi:10.1016/j.jsg.2014.07.009
Tanioka, Y., Satake, K., 1996. Fault parameters of the 1896 Sanriku Tsunami Earthquake estimated from Tsunami Numerical Modeling. Geophys. Res. Lett 23, 1549–1552. doi:10.1029/96GL01479
Ujiie, K., Tanaka, H., Saito, T., Tsutsumi, A., Mori, J.J., Kameda, J., Brodsky, E.E., Chester, F.M., Eguchi, N., Toczko, S., Expedition 343 and 343T Scientists, 2013. Low Coseismic Shear Stress on the Tohoku-Oki Megathrust Determined from Laboratory Experiments. Science 342, 1211–1214. doi:10.1126/science.1243485
Violay, M., Di Toro, G., Gibert, B., Nielsen, S., Spagnuolo, E., Del Gaudio, P., Azais, P., Scarlato, P.G., 2014. Effect of glass on the frictional behavior of basalts at seismic slip rates. Geophys. Res. Lett. 41, 348–355. doi:10.1002/ 2013GL058601
Wang, K., Hu, Y., 2006. Accretionary prisms in subduction earthquake cycles: The theory of dynamic Coulomb wedge. J. Geophys. Res. 111, B06410. doi:10.1029/2005JB004094
Wang, K., Hu, Y., Huene, von, R., Kukowski, N., 2010. Interplate earthquakes as a driver of shallow subduction erosion. Geology 38, 431–434. doi:10.1130/G30597.1
Yamanaka, Y., Kikuchi, M., 2004. Asperity map along the subduction zone in northeastern Japan inferred from regional seismic data. J. Geophys. Res. 109, 1–16. doi:10.1029/2003JB002683
Zheng, G., and Rice J., 1998. Conditions under which Velocity-Weakening Friction Allows a Self-healing versus a Cracklike Mode of Rupture, *BSSA*, *88, No. 6*, 1466–1483.

Acknowledgements: S.M., G.D.T., E.S., S.N., S.A. were supported by the European Research Council Consolidator Grant Project No. 614705 NOFEAR . S.L. and A.P were supported by the European Union's Seventh Framework Programme (FP7/2007-

2013) under grant agreement n° 603839 (Project ASTARTE - Assessment, Strategy and Risk Reduction for Tsunamis in Europe). All of the figures have been created using either MATLAB (www.mathworks.com) and Generic Mapping Tools (http://gmt.soest.hawaii.edu). Two anonymous reviewers and the Editor are acknowledged for their constructive comments which further improved the paper.

Author Contributions: S.M. performed the numerical simulations. G.D.T., E.S., S.A. and S.N. provided frictional parameters for numerical models from both experiments they performed and literature. F.R. digitised slip distributions from historical earthquakes. Tsunami source estimates provided by F.R. and A.S.; G.F. and A.S. developed the numerical code. Concept development: S.M., G.D.T., S.L. and E.S; important ideas provided by S.N., G.F. and A.P. throughout the development of the work. All authors contributed to text and revised the manuscript several times.

Additional Information

The authors declare no competing financial interests. Correspondence and requests for materials should be addressed to S.M. (shane.murphy@ifremer.fr).

Supplementary Material

Title: Tsunamigenic earthquake simulations using experimentally derived friction laws

S. Murphy[1,2*], G. Di Toro[3,4], F. Romano[1], A. Scala[1], S. Lorito[1], E. Spagnuolo[1], S. Aretusini[3], G. Festa[4], A. Piatanesi[1], S. Nielsen[5]

[1]Istituto Nazionale di Geofisica e Vulcanologia, Rome, Italy

[2]Ifremer, Plouzané, France

[3]University of Manchester, Manchester, United Kingdom

[4]Università degli Studi di Padova, Padua, Italy

[5]Università di Napoli Federico II, Naples, Italy

[6]Durham University, Durham United Kingdom

*shane.murphy@ifremer.fr

A1. Model Setup

	ρ (kg/m^3)	v_p (km/s)	v_s (km/s)	Colour in Fig. 1
Oceanic Mantle	3300	8.0	4.6	Purple
Oceanic	3000	7.3	4.4	Yellow
Lower Crust	3000	8.0	4.6	Blue
Middle Crust	2800	7.1	4.1	Red
Wedge	2500	4.7	2.1	Green
Continental / upper crust	2500	6.2	3.6	Gold
Oceanic Surface	2800	7.1	4.4	Brown

Table S1: Elastic parameters used in numerical model as depicted in Fig. 1 (main text).

No. of nodes per element face	9
dt	$1\ 10^{-3}$ s
Average element length along fault	2.47 km
Largest Courant No.	$6\ 10^{-3}$

Table S2: Numerical model parameters.

	Clay-like	Rock-like
μ_s	0.25	0.7
μ_d	0.1	0.2
α	3.7	78
β	1	1

Table S3: Frictional properties used for clay-like and rock-like materials. Rock-like frictional parameters are based on Del Gaudio et al.(2009) for peridotite (note that similar values are valid for gabbro, basalts and serpentinites, the most common rocks of the oceanic lithosphere). The thermal slip weakening friction law produces a similar evolution of stress with slip and roughly similar thermal weakening distances observed in thermal pressurization modelling for the Japanese trench(Hirono et al., 2016). See Methods for the clay-like materials frictional properties.

Run	V	σ_n	d_{th}	Ref.
	(m/s)	MPa	(m)	
HVR784	1.04	0.28	16.76	(Brantut et al., 2008)
HVR787	1.04	0.48	6.01	(Brantut et al., 2008)
HVR782	1.04	0.59	5.54	(Brantut et al., 2008)
HVR786	1.04	0.82	6.84	(Brantut et al., 2008)
HVR781	1.04	0.99	6.34	(Brantut et al., 2008)
HVR788	1.04	1.15	4.37	(Brantut et al., 2008)
HVR780	1.04	1.32	1.37	(Brantut et al., 2008)
HVR754	1.04	0.6	4.17	(Brantut et al., 2008)
HVR905	1.04	0.62	2.10	(Brantut et al., 2008)
1372	1.31	1	3.00	(Ferri et al., 2011)
1868	1.31	1	2.50	(Ferri et al., 2011)
405	1.3	9	0.06	(Bullock et al., 2015)
395	1.3	9	0.07	(Bullock et al., 2015)
820	1	4	0.07	(Proctor et al., 2014)
821	1	11.8	0.09	(Proctor et al., 2014)
822	1	17.8	0.06	(Proctor et al., 2014)
823	1.1	22.4	0.05	(Proctor et al., 2014)
745	1.2	8.3	0.08	(Proctor et al., 2014)
HVR178	1.03	0.66	7.50	(Mizoguchi et al., 2009)
HVR189	1.03	0.375	7.71	(Mizoguchi et al., 2009)
HVR190	1.03	0.345	11.39	(Mizoguchi et al., 2009)
HVR183	1.03	0.64	12.71	(Mizoguchi et al., 2009)
HVR184	1.03	0.636	8.89	(Mizoguchi et al., 2009)
HVR180	1.03	1.26	1.39	(Mizoguchi et al., 2009)
HVR185	1.03	1.289	2.20	(Mizoguchi et al., 2009)
HVR182	1.03	1.873	2.48	(Mizoguchi et al., 2009)
HVR188	1.03	1.856	1.83	(Mizoguchi et al., 2009)
LHV304	1.4	0.6	8.38	(Yao et al., 2013a)
LHV305	1.4	0.8	4.87	(Yao et al., 2013a)
LHV306	1.4	1	2.56	(Yao et al., 2013a)
LHV308	1.4	1.3	1.73	(Yao et al., 2013a)
LHV307	1.4	1.7	1.35	(Yao et al., 2013a)
LHV309	1.4	2.5	0.78	(Yao et al., 2013a)
LHV242	1.4	0.8	6.04	(Yao et al., 2013b)
LHV241	1.4	0.8	4.14	(Yao et al., 2013b)
LHV243	1.4	0.8	6.64	(Yao et al., 2013b)
LHV244	1.4	0.8	4.61	(Yao et al., 2013b)
LHV248	1.4	0.8	3.81	(Yao et al., 2013b)
LHV246	1.4	0.8	3.47	(Yao et al., 2013b)
LHV256	1.4	0.8	5.84	(Yao et al., 2013b)
LHV251	1.4	0.8	1.97	(Yao et al., 2013b)
LHV253	1.4	0.8	3.34	(Yao et al., 2013b)

LHV365	1.4	0.8	3.14	(Yao et al., 2013b)
HVR1489	1.3	1.01	0.23	(Togo et al., 2011)
HVR1490	1.3	0.8	3.25	(Togo et al., 2011)
HVR1491	1.3	0.61	4.14	(Togo et al., 2011)
HVR1494	1.3	1.21	1.51	(Togo et al., 2011)
HVR1496	1.3	1.64	1.63	(Togo et al., 2011)
HVR1497	1.3	2.05	1.22	(Togo et al., 2011)
HVR1502	1.3	3.04	0.63	(Togo et al., 2011)
s1168	1.3	5	0.18	(Aretusini et al., 2017)
s1167	1.3	5	0.10	(Aretusini et al., 2017)
s1166	1.3	5	0.64	(Aretusini et al., 2017)

Table S4: Source of experimential data plotted in Fig. 3.

Case Study Colour in Fig. 3	Max. shear stress depth (km)	Nucleation depth (km)
Deep	39	34
Intermediate	20	23
Shallow	17	14.5

Table S5: Model name and corresponding depth of maximum initial stress and nucleation.

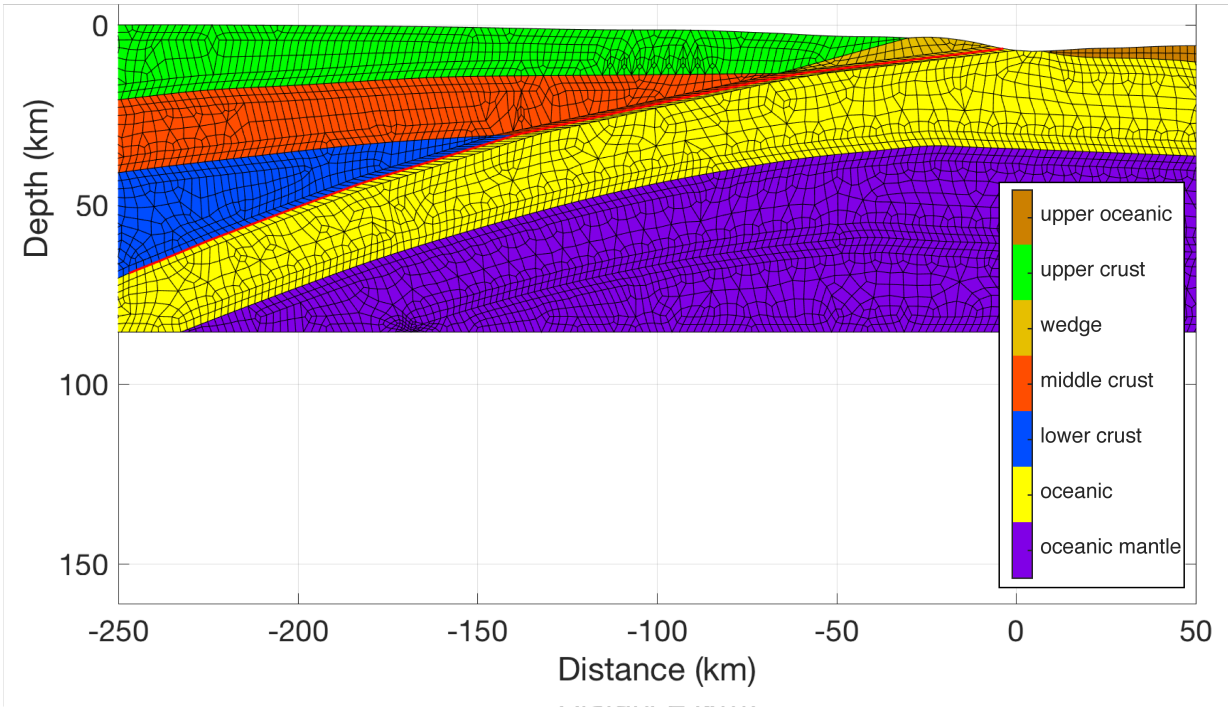

Figure S1: mesh used in simulations where boundary of cell is demarked by solid black line. Solid red line represents the fault. Colour coding of layers is the same as that used in Fig. 2 in main text.

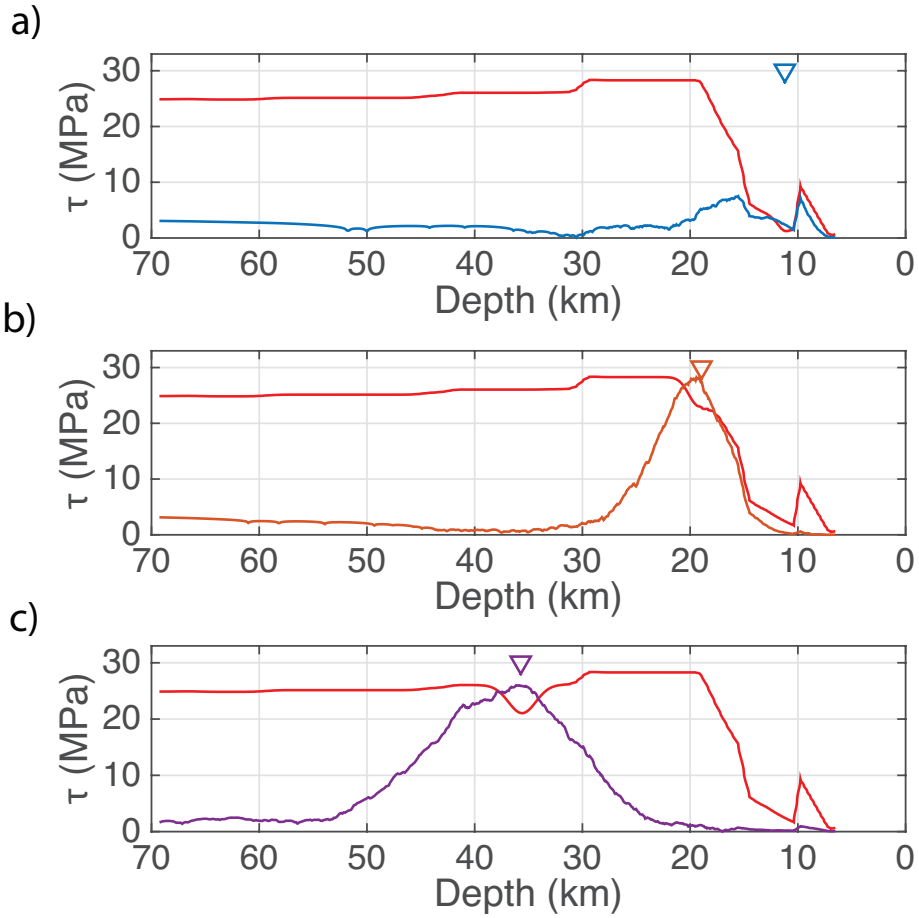

Figure S2: Initial stress (blue, orange, and purple lines) and yield stress (red line) containing nucleation depth (denoted by triangles). **a)** shallow, **b)** intermediate and **c)** deep case study simulations.

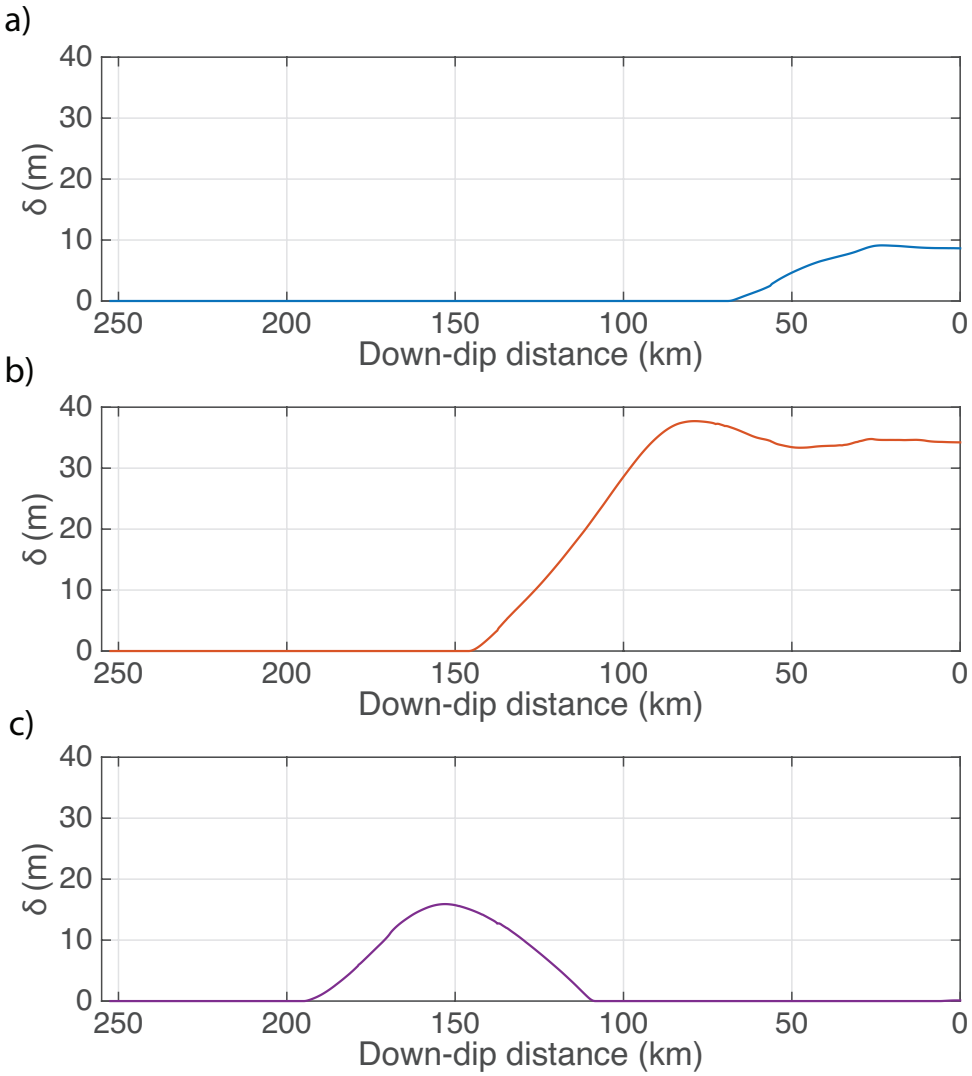

Figure S3: Final slip as a function of fault down-dip distance from the free surface (i.e., seafloor). **a)** shallow, **b)** intermediate and **c)** deep case study simulations (main text Fig. 2).

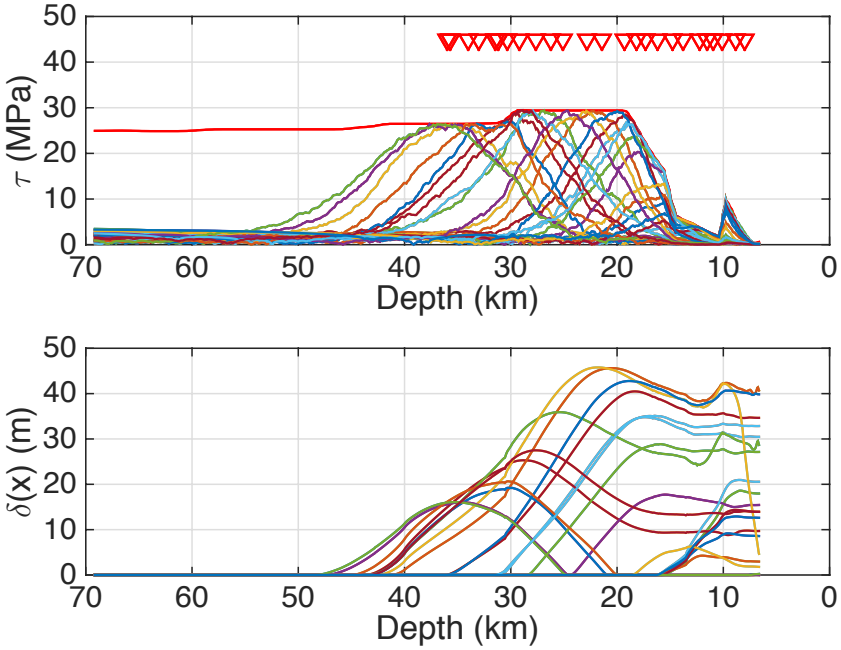

Figure S4: Initial stress (top subplot) and resulting slip distributions (bottom subplot) from the simulations plotted in Fig. 3 in the main text.

A2. Scaling between principal stresses

The shear and normal stress (τ and σ_n respectively) can be defined in terms of the principal stresses σ_1 and σ_2 where $\sigma_1 > \sigma_2$ as (Jaeger et al., 2007):

$$\tau = \frac{-(\sigma_1 + \sigma_2)}{2} \sin 2\theta \qquad \text{(Eqn. S1)}$$

$$\sigma_n = \frac{(\sigma_1 + \sigma_2)}{2} + \frac{(\sigma_1 - \sigma_2)}{2} \cos 2\theta \qquad \text{(Eqn. S2)}$$

θ is the anti-clockwise rotation from the direction of maximum principal stress to the normal of the fault plane which in the case of subduction zones is horizontal, the fault dip ϕ is therefore defined as $\phi = \theta - \pi/2$. Substituting Byleree's Law ($\tau = \mu\,\sigma_n$ where μ is the coefficient of friction) into Eqn S1 to replace τ, this new equation can be combined with Eqn S2 to give:

$$\sigma_1 = \left\{\frac{\sin(2\,\theta) + \mu\,\cos(2\,\theta) - \mu}{\mu + \mu\,\cos(2\,\theta) + \sin(2\,\theta)}\right\}\sigma_2 \qquad \text{(Eqn. S3)}$$

This equation provides a scaling relationship between the principal stress components based on the coefficient of friction and (indirectly) the fault dip. In our numerical model the static coefficient of friction varies from 0.25 at the surface to 0.7 at depth, similarly the fault geometry varies by a large amount. In the literature, Ma et al. (2012) (referenced in the manuscript) applied a value $\sigma_1 = 4.7545\,\sigma_2$ for subduction zone fault while Brace and Kohlstedt (1980) used a ratio of $\sigma_1 = 5\,\sigma_2$ in order to estimate a general estimate of lithospheric stress. We have taken a ratio of 4.05 which corresponds to fault dipping at 37° with a coefficient of friction of 0.7. It is also valid for a 10.6° fault dip with a coefficient of friction of 0.5.

A3. Tsunami Source

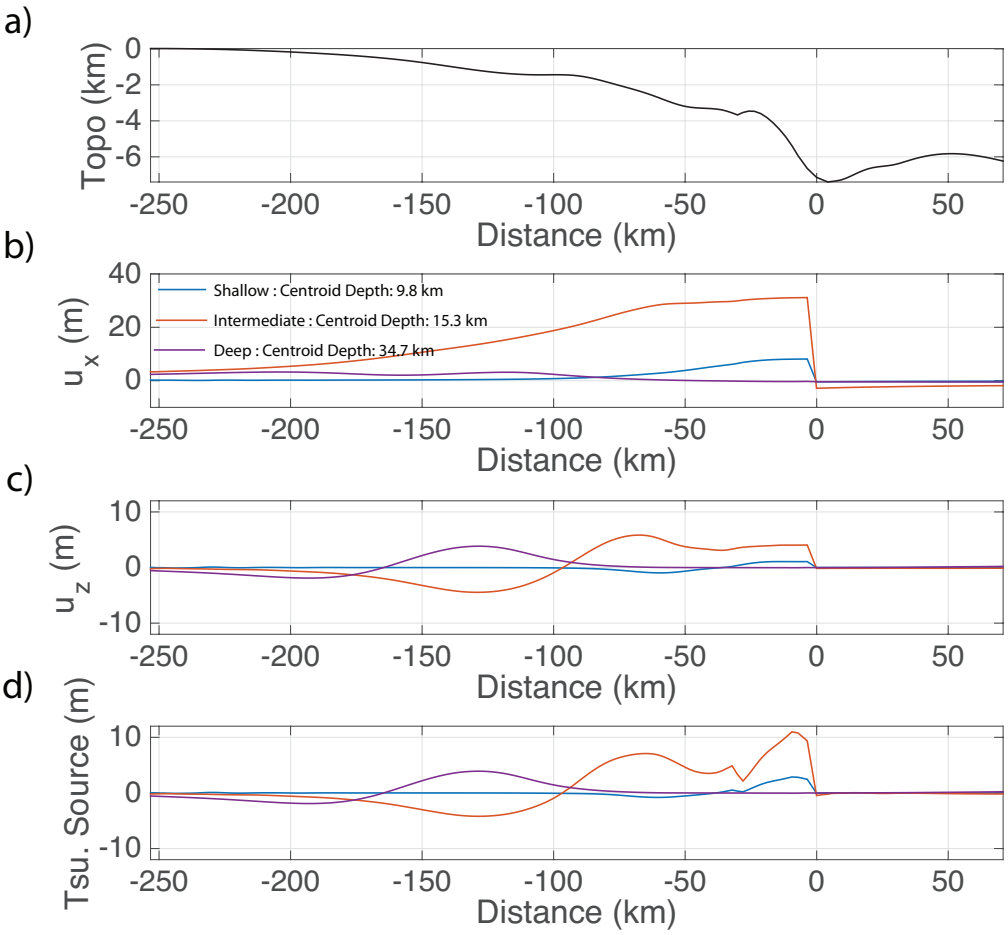

Figure S5: The displacement used for a tsunami source is based on the vertical seafloor displacement and the horizontal motion of the trench slope. It is calculated using the formula $d = u_z + \frac{\partial T}{\partial x} u_x$ where u_z and u_x and the vertical and horizontal seafloor displacements respectively and $\frac{\partial T}{\partial x}$ is the gradient of the water depth (Tanioka and Satake, 1996). **a)** is the seafloor depth in the numerical model, **b)** is the horizontal displacement in the three case study simulations, **c)** is the vertical seafloor displacement, and **d)** is the displacement accounted for in a tsunami source.

111

112

113 **A4. Calculation for 1-Dimensional normalised rupture duration and seismic**
114 **moment**

115 The normalised rupture duration is calculated in a similar manner to previous work
116 (Houston et al., 1998) however the change from a 2-D fault to a 1-D line fault needs
117 to be accounted for. In the case of this work the moment M_o for a 1-D line is defined
118 as:

119

$$M_o = G\ W\ \bar{\delta} \qquad \text{(Eqn. S4)}$$

120

121

122 where G the shear modulus, W the fault rupture width and $\bar{\delta}$ the average slip(Mitsui
123 and Yagi, 2013). The average slip can also be defined in terms of the average static
124 stress drop, $\Delta\sigma$:

125

$$\bar{\delta} = \mathrm{C}\frac{\Delta\sigma}{G}L \qquad \text{(Eqn. S5)}$$

126

127

128 where C is a constant and L is the rupture length. Setting the L equal to W, and
129 substituting it in terms of rupture duration (i.e., $W = T\ v_r$, where T is rupture duration
130 and v_r is rupture velocity). Combining Equations S1, S2 and substituting in the
131 duration in place of the width produces:

132

$$T = \frac{1}{v_r}\sqrt{\frac{M_o}{\mathrm{C}\ \Delta\sigma}} \qquad \text{(Eqn. S6)}$$

133

134

This is different for the 2-D case (i.e., $T \propto {M_o}^{1/3}$). Therefore, normalising the 1-D duration to a given reference moment, M_o^{ref}, is defined as:

$$T_N^{1D} = T\left(\frac{M_o}{M_o^{ref}}\right)^{1/2} \qquad \text{(Eqn. S7)}$$

For the normalised duration for observations (Bilek and Lay, 1999) M_o^{ref} was set to a magnitude 6 event. To make our numerical results comparable to these observations, we calculated the slip distribution of a circular asperity of M 6 and calculated the moment along a line through the centre of the asperity. This gave a value of 3.7 10^{14} Pa m^2 which M_o^{ref} was set equal to in Eqn. S7.

A5. Sensitivity Analysis: depth at which fluid retention depth occurs

Two additional ensembles were run where the fluid retention depth, z_{FRD}, was shifted ± 5km of the original depth, that is depths of 7 km and 17 km. The effect on yield stress and initial stress distributions, is depicted in Fig. S6 for z_{FRD} = 7 km, and in Fig. S7 for z_{FRD} = 17 km. In both cases 15 simulations were performed. Fig. S8 shows the comparison between the three ensembles in terms of moment, average static stress drop, normalised rupture duration, average breakdown energy, average slip-rate per earthquake and average rupture velocity. Fig. S8 shows that the earthquakes in the ensemble with z_{FRD} = 17 km are similar to case in the main text (i.e., z_{FRD} = 12 km), however the depth dependent trends are different in the case with z_{FRD} = 7 km.

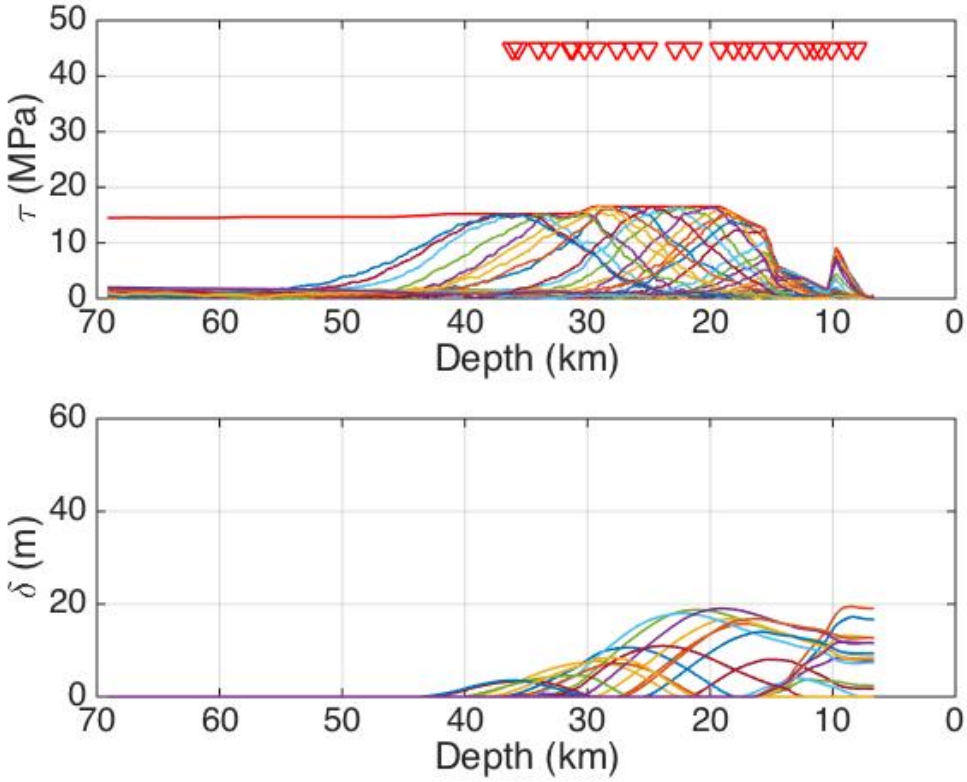

Figure S6: Initial stress (top subplot) and resulting slip distributions (bottom subplot) in the z_{FRD} = 7 km case. In the top subplot the red line is the yield stress and each coloured line is an initial stress distribution used in an individual simulation. The green triangles denote the location of seismic rupture nucleation. In the bottom subplot the colour code of the slip distributions match colour code used for the initial stress distributions used in the subplot above.

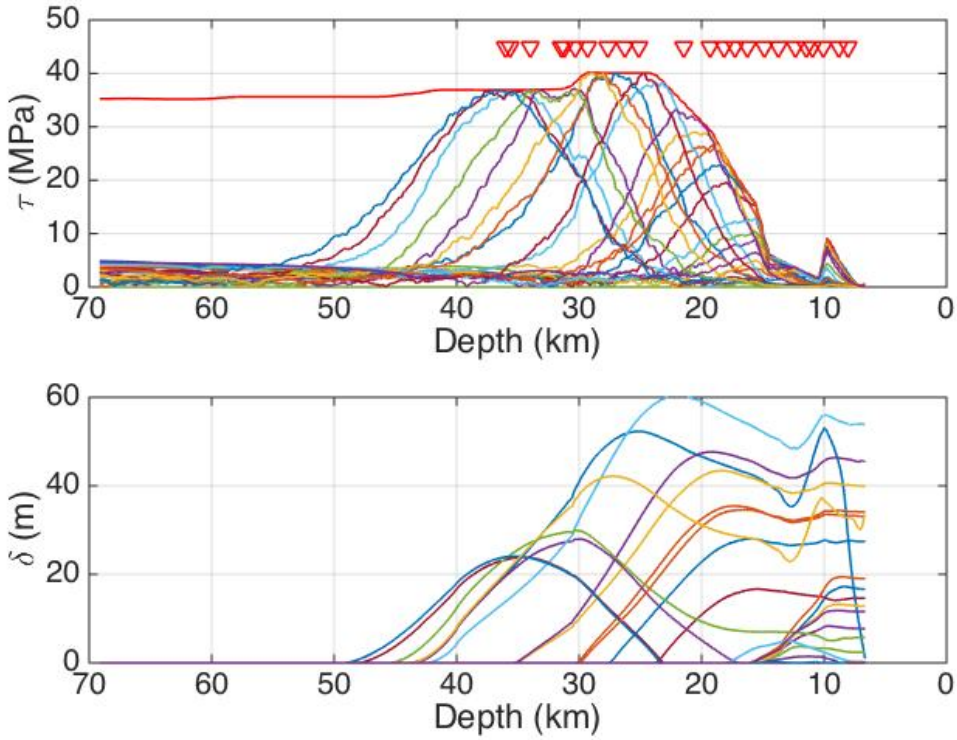

Figure S7: Initial stress (top subplot) and resulting slip distributions (bottom subplot) in the z_{FRD} = 17 km case. In the top subplot the red line is the yield stress and each coloured line is an initial stress distribution used in an individual simulation. The green triangles denote the location of the seismic rupture nucleation. In the bottom subplot the colour code of the slip distributions match colour code used for the initial stress distributions used in the subplot above.

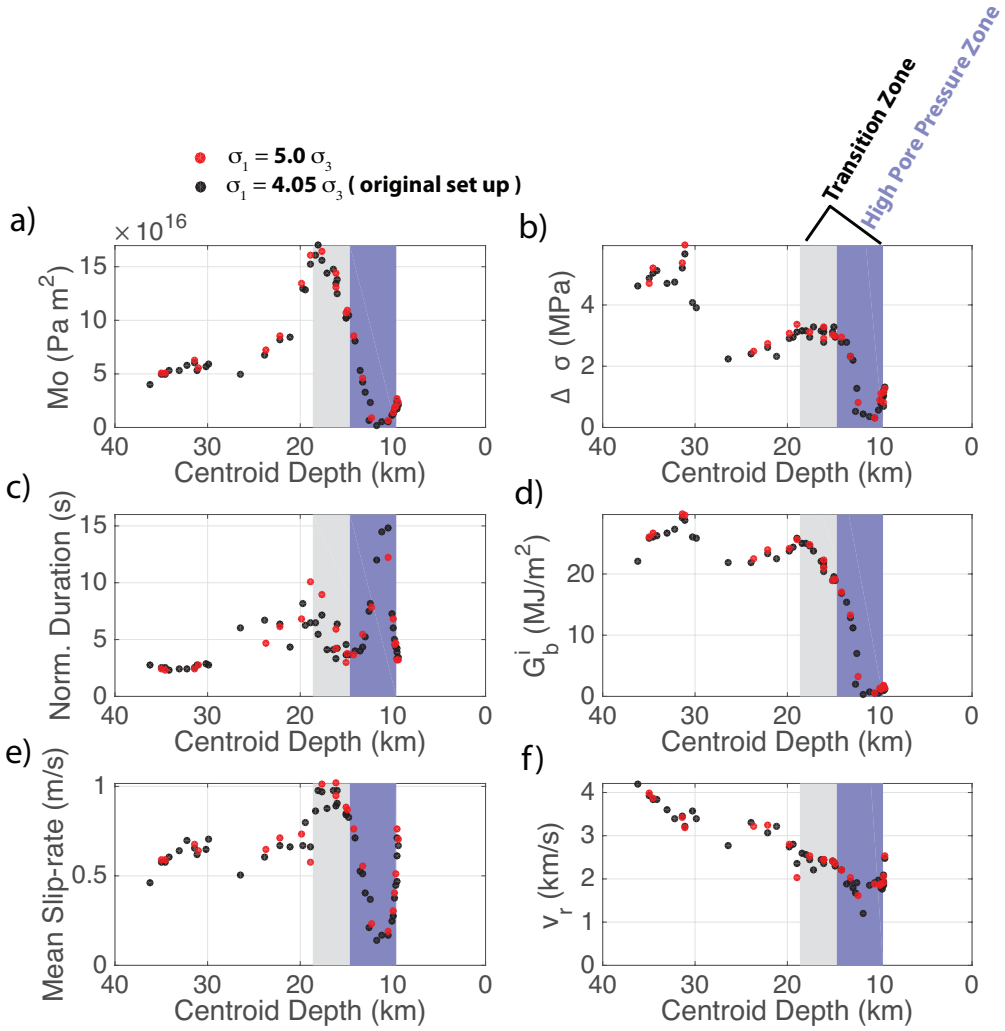

Figure S8: Testing the effect of changing the relationship between the principal components of stress. Black dots are for the simulations as described in the main text, that is $\sigma_1 = 4.05\ \sigma_3$, while red dots are for $\sigma_1 = 5.0\ \sigma_3$. **a)** Seismic moment of the 1-D line earthquake; a constant $G = 30$ GPa rather than a depth dependent shear modulus was used in the calculation as is commonly used in observational seismology. **b)** Average static stress drop; **c)** normalised rupture duration; **d)** average breakdown energy; **e)** average slip-rate per earthquake and **f)** average rupture velocity.

A6. Averaged rupture features for 3 case studies.

	Shallow	Intermediate	Deep
G_b^i (MJ/m^2)	1.15	19.6	25.8
$\Delta\sigma$ (MPa)	0.96	3.0	4.76
v_r (km/s)	1.7	2.5	3.9
T_r (s)	22.6	31.6	18.6
$\dot{\delta}$ (m/s)	0.24	0.65	0.41

Table S6: Earthquake source parameters for four simulated ruptures reported in Fig. 2 of the main text. Average breakdown energy G_b^i based on the assumed slip weakening friction law (Eq. S1), the numerical integration of stress (Eq. S2) and the average static stress drop. In all cases only points where coseismic slip occurs are considered when calculating the mean breakdown energy and static stress drop. v_r is the average rupture velocity, T_r is the average rise time and $\dot{\delta}$ is the average slip-rate on the fault. All averaged values are based on section of the fault that slips.

References

Bilek, S.L., Lay, T., 1999. Rigidity variations with depth along interplate megathrust faults in subduction zones. Nature 400, 443–446. doi:10.1038/22739

Brace, W.F., Kohlstedt, D.L., 1980. Limits on lithospheric stress imposed by laboratory experiments. Journal of Geophysical Research: Solid Earth (1978–2012) 85, 6248–6252. doi:10.1029/JB085iB11p06248

Brantut, N., Schubnel, A., Rouzaud, J.N., Brunet, F., Shimamoto, T., 2008. High-velocity frictional properties of a clay-bearing fault gouge and implications for earthquake mechanics. Journal of Geophysical Research: Solid Earth (1978–2012) 113, B10401. doi:10.1029/2007JB005551

Bullock, R.J., De Paola, N., Holdsworth, R.E., 2015. An experimental investigation into the role of phyllosilicate content on earthquake propagation during seismic slip in carbonate faults. J Geophys Res-Sol Ea 120, 3187–3207. doi:10.1002/2015JB011914

Del Gaudio, P., Di Toro, G., Han, R., Hirose, T., Nielsen, S., Shimamoto, T., Cavallo, A., 2009. Frictional melting of peridotite and seismic slip. Journal of Geophysical Research 114, B06306–19. doi:10.1029/2008JB005990

Ferri, F., Di Toro, G., Hirose, T., Han, R., Noda, H., Shimamoto, T., Quaresimin, M., de Rossi, N., 2011. Low- to high-velocity frictional properties of the clay-rich gouges from the slipping zone of the 1963 Vaiont slide, northern Italy. Journal of Geophysical Research: Solid Earth (1978–2012) 116, B09208. doi:10.1029/2011JB008338

Hirono, T., Tsuda, K., Tanikawa, W., Ampuero, J.-P., Shibazaki, B., Kinoshita, M., Mori, J.J., 2016. Near-trench slip potential of megaquakes evaluated from fault properties and conditions. Sci. Rep. 1–13. doi:10.1038/srep28184

Houston, H., Benz, H.M., Vidale, J.E., 1998. Time functions of deep earthquakes from broadband and short-period stacks. J Geophys Res-Sol Ea 103, 29895–29913. doi:10.1038/ncomms3606

Jaeger, J.C., Cook, N., Zimmerman, R., 2007. Fundamentals of rock mechanics.

Ma, S., 2012. A self-consistent mechanism for slow dynamic deformation and tsunami generation for earthquakes in the shallow subduction zone. Geophys. Res. Lett 39, n/a–n/a. doi:10.1029/2012GL051854

Mitsui, Y., Yagi, Y., 2013. An interpretation of tsunami earthquake based on a simple dynamic model: Failure of shallow megathrust earthquake. Geophys. Res. Lett 40, 1523–1527. doi:10.1002/grl.50266

Mizoguchi, K., Hirose, T., Shimamoto, T., Fukuyama, E., 2009. High-velocity frictional behavior and microstructure evolution of fault gouge obtained from Nojima fault, southwest Japan. Tectonophysics 471, 285–296. doi:10.1016/j.tecto.2009.02.033

Proctor, B.P., Mitchell, T.M., Hirth, G., Goldsby, D., Zorzi, F., Platt, J.D., Di Toro, G., 2014. Dynamic weakening of serpentinite gouges and bare surfaces at seismic slip rates. J Geophys Res-Sol Ea 119, 8107–8131. doi:10.1002/2014JB011057

Tanioka, Y., Satake, K., 1996. Tsunami generation by horizontal displacement of ocean bottom. Geophys. Res. Lett 23, 861–864. doi:10.1029/96GL00736

Togo, T., Shimamoto, T., Ma, S., Hirose, T., 2011. High-velocity frictional behavior of Longmenshan fault gouge from Hongkou outcrop and its implications for dynamic weakening of fault during the 2008 Wenchuan earthquake. Earthq Sci

24, 267–281. doi:10.1007/s11589-011-0790-6
Yao, L., Ma, S., Shimamoto, T., Togo, T., 2013a. Structures and high-velocity frictional properties of the Pingxi fault zone in the Longmenshan fault system, Sichuan, China, activated during the 2008 Wenchuan earthquake. Tectonophysics 599, 135–156. doi:10.1016/j.tecto.2013.04.011
Yao, L., Shimamoto, T., Ma, S., Han, R., Mizoguchi, K., 2013b. Rapid postseismic strength recovery of Pingxi fault gouge from the Longmenshan fault system: Experiments and implications for the mechanisms of high-velocity weakening of faults. J Geophys Res-Sol Ea 118, 4547–4563. doi:10.1002/jgrb.50308